Surrogate optimization of a lattice foot orthotic

Mohammadreza Moeini[a], **Lingyu Yue**[a],
Mickael Begon[b], **Martin Lévesque**[a,*]

[a] *Laboratory for Multiscale Mechanics, Polytechnique de Montréal, Montréal, Québec H3C3A7, Canada*

[b] *Laboratory of Simulation and Movement Modelling, School of Kinesiology and Physical Activity Sciences, Québec, Canada. CHU Sainte-Justine - Research Center, Québec, Canada.*

Abstract

Background: Additive manufacturing enables to print patient-specific Foot Orthotics (FOs). In FOs featuring lattice structures, the variation of the cell's dimensions provides a locally variable stiffness to meet the therapeutic needs of each patient. In an optimization problem, however, using explicit Finite Element (FE) simulation of lattice FOs with converged 3D elements is computationally prohibitive. This paper presents a framework to efficiently optimize the cell's dimensions of a honeycomb lattice FO for flat foot condition. **Methods:** We built a surrogate based on shell elements whose mechanical properties were computed by the numerical homogenization technique. The model was submitted to a static pressure distribution of a flat foot and it predicted the displacement field for a given set of geometrical parameters of the honeycomb FO. This FE simulation was considered as a black-box and a derivative-free optimization solver was employed. The cost function was defined based on the difference between the predicted displacement by the model against a therapeutic target displacement. **Results:** Using the homogenized model as a surrogate significantly accelerated the stiffness optimization of the lattice FO. The homogenized model could predict the displacement field 78 times faster than the explicit model. When 2000 evaluations were required in an optimization problem, the computational time was reduced from 34 days to 10 hours using the homogenized model rather than explicit model. Moreover, in the homogenized model, there was no need to re-create and re-mesh the insole's geometry in each iteration of the optimization. It was only required to update the effective properties. **Conclusion:** The presented homogenized model can be used as a surrogate within an optimization framework to customize cell's dimensions of honeycomb lattice FO in a computationally efficient manner.

Keywords: Foot Orthotics, Flat Foot, Finite Element Method, Derivative-free Optimization, Homogenization, Surrogate

Highlights

- We presented a surrogate optimization of a honeycomb lattice foot orthotic.
- The cost function was reaching a target deflection of the foot orthotic.
- The variables were the geometrical parameters of the honeycomb lattice.
- The difference between the solutions and the target was less than 0.5 mm.
- The surrogate reduces the computational time from 34 days to 10 hours.

1 Introduction

A *flat foot* is characterized by a loss of dynamic and static support of the medial longitudinal arch. It has a prevalence of 20-25% in the adult population [1]. This foot deformity affects the walking function as well as the alignment of the ankle (*i.e.,* excessive foot pronation), knee and hip joints [2, 3]. Prescription of foot orthotics (FOs) is one of the most common treatment to prevent pain and overuse injuries [4,5]. Moreover, customized FOs enable better control of excessive foot pronation and provide better comfort for patients than prefabricated FOs [6–8]. Additive manufacturing has paved the way to rapidly manufacture patient-specific and affordable FOs with customized mechanical properties [9, 10]. In 3D printed lattice FOs, the cell dimensions are locally varied to build a functionally-graded lattice structure whose mechanical response satisfies the therapeutic needs.

Yet, the remaining challenge is how to find the best variation of the cells dimensions to meet the therapeutic needs. This question can be answered by model developers within an optimization problem based on the predictions of a Finite Element (FE) simulation of the lattice structure under representative loading and boundary conditions [11, 12]. The therapeutic needs of the patients, on the other hand, should be addressed by clinicians. Desmyttere et al. [4], for instance, reported that, in general, the key is to avoid the excessive collapse of the longitudinal arch to deliver an efficient propulsion during gait. Nevertheless, the flat foot condition includes a broad spectrum of clinical pathologies. Many medical tests are required to accurately determine the appropriate therapy for each patient [13]. The prescribed therapy is usually based on the morphological parameters of the foot. These parameters can be identified by footprint evaluations, anthropometric measures, gait analysis in laboratory or simply through a visual inspection in clinical practice [14]. Thus, the whole designing process of customized FOs depends on the clinical data and the experience of the orthotists [15]. The structural optimization features (*e.g.*, the cost functions, variables, constraints, etc.) as well as the optimized solution, correspondingly, should be frequently updated and interpreted for each patient receiving clinical feedback from orthotists. To

speed up this process, there is a need for a computationally fast, robust, and easy-to-use optimization tool to help orthotists make decisions and design customized lattice FOs to correct the flat foot condition.

In this paper, we have introduced a computationally efficient simulation-based optimization framework to design honeycomb lattice FOs for flat feet. Although we have not proposed any specific treatment, the presented optimization procedure could be employed to rapidly provide the best honeycomb cells dimensions to control the FO's deflections under any given pressure distribution of a flat foot.

2 Background and methods

This section presents the *Numerical Homogenization* technique and the *Derivative-free* algorithms to build a computationally efficient FE model and the optimization framework. It also presents our designed honeycomb FO and introduces six examples where the geometrical parameters of this FO were optimized. All examples consist of previously known solutions to assess the performance of the surrogate in terms of computational cost and accuracy. Note that, in this study, a vector is denoted by a boldface letter (*e.g.*, $\mathbf{x}$).

2.1 Simulation-based optimization problems

In simulation-based optimization problems, the cost function is an outcome of a computer simulation (so called *Black-box*) which might also be computationally expensive. In black-box optimization, it is assumed that there is no information about the gradient of the cost function. The optimized solution is found by evaluating the black-box output and updating its input, iteratively. In our case, the 3D printed FO should be sufficiently rigid to support the medial longitudinal arch of a flat foot (Figure 1). The FE simulation output of interest, therefore, is the predicted displacement field when the FO is subjected to a static pressure distribution of a flat foot. However, when a lattice FO is explicitly meshed by 3D solid elements (so called *explicit model*), the FE simulation requires at least 10^6 elements to provide a converged solution [16]. Iteratively running such a complex FE simulation would be inevitably computationally expensive because, in black-box optimization, more than 1000 evaluations are usually required to reach a minimum [17–19]. The computational cost, however, can be significantly reduced by a surrogate optimization.

2.2 Surrogate optimization by the homogenization technique

When the cost function is computationally expensive, it can be replaced by a more efficient function so called *Surrogate*. The surrogate should provide a close, but not necessarily the

exact, local minimum [18]. In a lattice structure, the surrogate can be provided by the homogenization technique [20–23]

The homogenization technique delivers the effective mechanical properties of heterogeneous materials such that the homogenized model predicts almost the same mechanical response as the heterogeneous structure. In numerical homogenization, a Representative Volume Element (RVE) of the heterogeneous material is explicitly meshed, a set of periodic boundary conditions are applied, and six orthogonal strain tensors are exerted over the RVE to find all the six columns of the effective stiffness tensor $\bar{C}_{ijkl}$ [24]. The honeycomb cell has three symmetrical planes and is orthotropic [25]. Its effective stiffness tensor $\bar{C}_{ijkl}$ [24] can be represented by the engineering constants (*i.e.*, $E_{11}, E_{22}, E_{33}, G_{12}, G_{13}, G_{23}, \nu_{12}, \nu_{13}$, and ν_{23}). We have already verified and experimentally validated the computed effective properties of a honeycomb cell using the above procedure in [25]. Moreover, we verified and validated the homogenized FE model of a honeycomb cellular FO in [16]. This FE model was employed in this study to customize the stiffness of honeycomb lattice FOs within a simulation-based optimization problem and using a derivative-free optimization algorithm.

2.3 Derivative-free optimization algorithms

In derivative-free optimization algorithms, there is no need to compute the gradient of the cost function which is suitable to solve the simulation-based optimization problems [18]. Mesh Adaptive Direct Search (MADS) is a derivative-free optimization algorithm to solve either single or bi-objective optimization problems [26]. MADS is a direct search method that finds the optimum by evaluating the black-box output at some trial points lying on the mesh. The algorithm starts by discretizing the domain with a mesh size of Δ^m and setting a frame with a poll size of Δ^p. The frame is moving through the space variables while the trial points are selected from its inside and the objective is evaluated at those points. Simultaneously, the mesh size and the poll size are dynamically updated at each iteration. This feature could potentially help the algorithm to evade local minima. The convergence proof of MADS

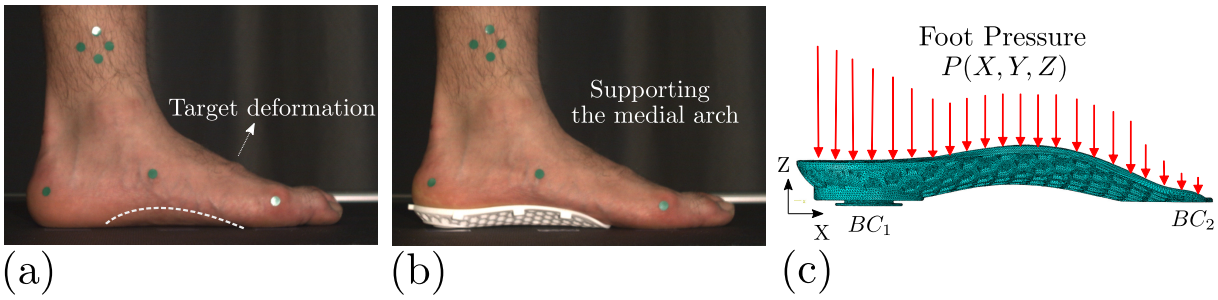

Figure 1: Simulation of a FO under the pressure distribution of a foot; (a) a flat foot, (b) a flat foot over a 3D printed honeycomb lattice FO. The FO supports the medial longitudinal arch of the foot. (c) Explicit FE simulation of the FO having 3D solid elements under the foot pressure distribution ($P(X, Y, Z)$), while the boundary conditions are applied on the heel part (BC_1) and on the fore foot (BC_2). The objective is to design the FO's geometrical parameters such that, when it is submitted to the foot pressure, it exhibits a target deflection. The designing process requires to solve a simulation-based optimization problem.

was presented in [18]. NOMAD (Nonlinear Optimization by Mesh Adaptive Direct Search) is also an open-source `C++` implementation of MADS algorithm to solve simulation-based optimization problems [27, 28].

2.4 Building the surrogate

2.4.1 Geometrical details of the designed foot orthotics

Figure 2 shows the designed lattice FO which was a lattice structure consisting of two layers; an infilled layer with a distribution of circular holes and a reinforced layer made of a honeycomb cellular structure. The holes were needed for ventilation functions during walking. The overall geometrical parameters were T_1, T_2 and L, which represented the height at the Lateral Longitudinal Arch (LLA), the height at Medial Longitudinal Arch (MLA), and the total length of the FO, respectively (Figure 2a). These parameters impact also on the curvature of the FO at the MLA and the LLA. Thus, they affect the overall stiffness of the FO, and correspondingly affect the resulting displacement when the FO is under the pressure distribution of the foot. In this research, we chose them arbitrarily and along with the previous studies [10, 29, 30]. Therefore, they were not treated as optimization variables,

and they remained constant as per $T_1 = 19.6\,\text{mm}$, $T_2 = 23.0\,\text{mm}$, $L = 170.0\,\text{mm}$. The surrogate model (Figure 2b) is a simplified geometry of the honeycomb lattice FO having the same topology, but with a continuous surface and featuring a variable local stiffness. The variable local stiffness comes from the variation of the local geometrical parameters. These parameters (Figure 2c) are the height of the infilled layer (h_1), the height of the honeycomb layer (h_2), the diameter of the circular holes (d), the horizontal and inclined hexagon side lengths (h_b and l_b), the wall thickness (t) and the angle between the vertical and inclined hexagon sides (θ). The hexagon outer side lengths (l and h) can be explicitly computed by $l = l_b + t/2\cos\theta$ and $h = h_b + t(1 - \sin\theta)/\cos\theta$. Using these geometrical parameters, the relative density, ρ, for a honeycomb unit cell is computed as per [31]:

$$\rho = 1 - \frac{l_b(h_b + l_b\sin\theta)}{l(h + l\sin\theta)}. \tag{1}$$

Parameters ρ and h_2 were locally varied to provide a variable stiffness. The other parameters (*i.e.*, h_1, d, θ), however, were considered to be constant to reduce the number of optimization variables. In this way, the parameters h_1 and d were fixed and arbitrarily assigned as per $h_1 = 1.5\,\text{mm}$ and $d = 0.75\,\text{mm}$. Moreover, only regular hexagons were considered in which $l_b = h_b$, $l = h$ and $\theta = \pi/6$.

2.4.2 Numerical homogenization of the honeycomb cells

The effective properties of the honeycomb unit cells were computed as a function of the relative density by the numerical homogenization technique (Algorithm 1). A unit cell was considered to be the RVE of the whole lattice structure. The numerical homogenization was conducted using `Abaqus` (version 6.14) FE software. The material of the RVE was assumed to be a linearly elastic and isotropic, and had a Young's modulus of E_{solid} and a Poisson's ratio of ν_{solid}. A comparatively very soft material, named as *elastic air* and having $E_{\text{void}} \ll E_{\text{solid}}$ and $\nu_{\text{void}} \simeq \nu_{\text{solid}}$, was attributed to the void phase to compute the macro-strain and macro-stress through volume integration [25]. The effective engineering

constants were computed for a honeycomb cell having relative densities $\rho = 10\% - 80\%$ with 10% increments. A continuous regression function using a polynomial interpolation (*i.e.*, $\sum_{i=0}^{n} \Theta_i \rho^i$) was then obtained through these points to compute the effective properties for any arbitrary $10\% \leq \rho \leq 80\%$ during the optimization process.

2.4.3 Mesh and Material properties

The homogenized FO consisted of quadratic shell elements (*i.e.*, `S8R5` element having 8 nodes and 5 degrees of freedom at each node) whose effective properties were computed from the numerical homogenization of a honeycomb cell whose constituting material had a Young's

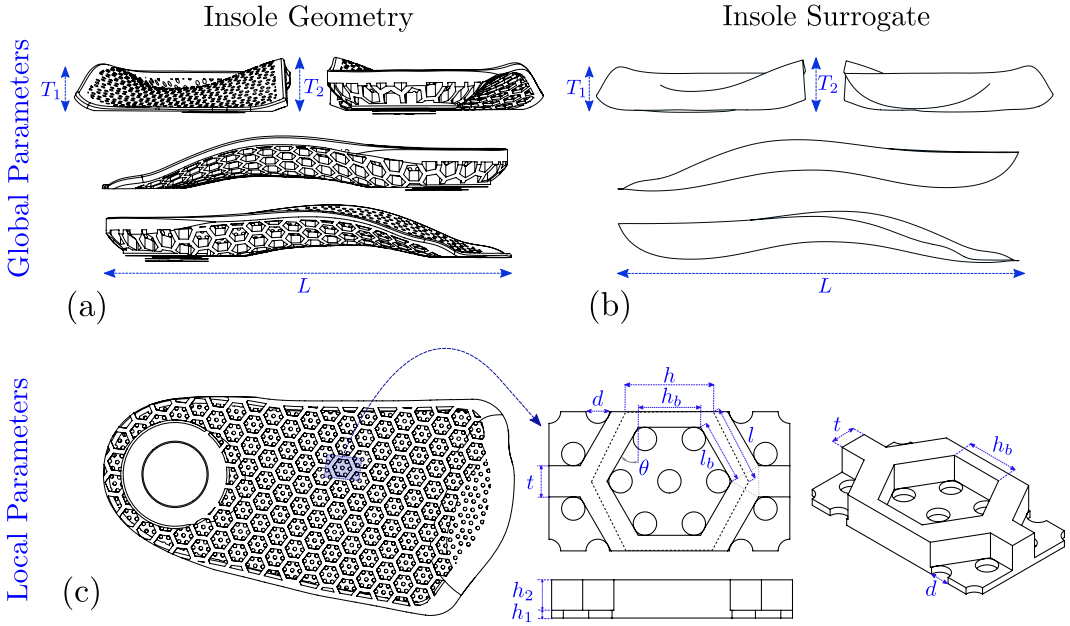

Figure 2: Schematic representation of the honeycomb lattice FO; (a) FO geometry having the global geometrical parameters of T_1 (the height at the lateral longitudinal arch), T_2 (the height at the medial longitudinal arch), and L (the total length of the FO), (b) surrogate of the detailed problem which is a simplified geometry of the FO with the same global geometrical parameters but for which the shell effective properties are obtained from numerical homogenization, (c) FO local geometrical parameters including the height of the infilled layer (h_1), the height of the honeycomb layer (h_2), the diameter of the circular holes (d), the horizontal and inclined hexagon side lengths (h_b and l_b) and the wall thickness (t). The relative density (ρ) is computed from Equation 1. Parameters ρ and h_2 are optimized to provide the required stiffness in this lattice FO. The other parameters are considered to be constant with $h_1 = 1.5\,\text{mm}$ and $d = 0.75\,\text{mm}$. Also, only a regular hexagonal cell was considered in which $l_b = h_b$, $l = h$ and $\theta = \pi/6$.

Algorithm 1: Computation of the effective properties

Simulation parameters
$(E_{\text{solid}}, \nu_{\text{solid}})$: Young's modulus and Poisson's ratio of the solid phase.
$(E_{\text{void}}, \nu_{\text{void}})$: Young's modulus and Poisson's ratio of the void phase (*elastic air*).
Process
for $\rho \in \{10, 20, \cdots, 80\}$ **do**
    Generate the RVE (one unit cell).
    Mesh the RVE
    Assign $(E_{\text{solid}}, \nu_{\text{solid}})$ and $(E_{\text{air}}, \nu_{\text{air}})$ to the solid and void phases.
    Apply periodic boundary conditions.
    Apply six orthogonal macro-strains.
    Compute the macro-stress $\mathbf{\Sigma} = \frac{1}{V}\int \boldsymbol{\sigma} \mathrm{d}V$ over the entire volume (V)
    Compute the macro-strain $\mathbf{E} = \frac{1}{V}\int \boldsymbol{\varepsilon} \mathrm{d}V$ over the entire volume (V)
    Compute the effective stiffness tensor $\bar{C}_{ijkl}$ by solving $\mathbf{\Sigma} = \tilde{\mathbf{C}} : \mathbf{E}$ for $\tilde{\mathbf{C}}$
    Compute the engineering constants $\bar{E}_{ii}$, $\bar{G}_{ij}$ and ν_{ij}.
Provide a continuous polynomial regression function ($\bar{E}_{ii}(\rho)$, $\bar{G}_{ij}(\rho)$ and $\nu_{ij}(\rho)$).

modulus of $E_s = 2055.63\,\text{MPa}$ and a Poisson's ratio of $\nu_s = 0.37$. These properties were extracted from Selective Laser Sintering (SLS) 3D printed Nylon-12 dog-bone specimens mechanically tested according to the `ASTM-D638` standard [16].

2.4.4 Boundary conditions and loading

The FO was subjected to a static pressure distribution of a flat foot ($P(X, Y, Z)$). This pressure was measured during a gait analysis of a 21-year-old female participant having a Body Mass Index (BMI) of 21.2 (height of 164 cm and weight of 57 kg), a shoe size of 8 US, arch height flexibility of 28 (right foot), arch height of 55.3 mm (right foot), and foot posture index of +6. The feet pressure distributions were measured using plantar pressure insoles (*Medilogic WLAN*, Germany) on the plantar surfaces of the FOs and during 23 walking cycles. The sensors recorded pressure distributions with a frequency of 400 Hz. Consequently, the measured plantar pressure consisted of 23 walking cycles normalized to 101 time frames. The pressure distribution of time frame 50, which corresponds to the pressure at the mid-stance phase, was selected and the mean pressure distribution was then computed from the 23 cycles. This pressure distribution was employed as a static loading in the FE simulation.

The boundary conditions were applied on the heel and the forefoot. In the heel part, all degrees of freedom were fixed while in the forefoot, only the out-of-plane displacement was fixed. These boundary conditions are a simplification of the interaction between the FO, the foot and the shoe. Nevertheless, it might be acceptable in a quasi-static simulation in which the goal is to only predict the FO's deformation at the mid-stance phase.

2.4.5 Verification of the surrogate's predictions

The verification of the surrogate's predictions consisted of three assessments. In the first assessment (Appendix A), the performance of the homogenized model was verified by the predictions of the explicit model assuming that the explicit model results in an exact solution (this assumption was verified and validated in our previous research works [16, 25]). Particularly, the predicted displacement field by the homogenized model was compared with the predictions of the explicit model over the top surface of the FO. In this comparison, we reported the relative difference between the predictions normalized by the maximum predicted U_Z by the explicit model (*i.e.*, $\frac{|U_Z^{\mathrm{Hmg}} - U_Z^{\mathrm{E}}|}{\max |U_Z^{\mathrm{E}}|}$). Moreover, the predictions were compared over three vertical lines and three horizontal lines on the top surface of the FO. In this comparison, the metric $\xi = \left| \frac{\max |U_Z^{\mathrm{Hmg}}| - \max |U_Z^{\mathrm{E}}|}{||U_Z^{\mathrm{E}}||_2} \right|$ was defined and reported for each line. Furthermore, the predicted arguments of the minimums (*i.e.*, argmin) over the selected lines were also mentioned. These values are reported to evaluate the performance of the homogenized model to predict the local minimum of the out-of-plane displacement, when compared to the prediction of the explicit model. In the second assessment (Appendix B), the convergence of the mesh size of both models was studied. In the third assessment, the computational time and the required memory to run the simulations were reported on a personal computer Intel® Core™ i7-8700K CPU @ 3.7 GHz and 64 GB RAM. The computational costs of the explicit and the homogenized models were compared together to assess the efficiency of the surrogate within the optimization procedure.

Algorithm 2: Simulation of the Foot Orthotic

Simulation parameters
l_{element}: Element's size.
E, ν: Young's modulus and Poisson's ratio.
(h_1, θ, d): Constant geometrical parameters.
$P(X, Y, Z)$: Pressure distribution of the foot.
(BC_1, BC_2): Boundary conditions at the heel and forefoot.
Process
Import the geometry.
Mesh the geometry.
Read the input ρ and h_2 from a `text` file.
Compute the effective properties using the regression function.
Assign the effective material properties to the model.
Assign the shell thickness h_2 to the model.
Apply the boundary conditions (BC_1, BC_2).
Apply the foot pressure distribution $P(X, Y, Z)$.
Solve the FE problem.
Save the displacement field U_Z into a `csv` file.

2.5 Optimization procedure

A python/shell code was written to run `Abaqus` (the simulator) for a given input and to return the output as the cost function to NOMAD (the optimizer). NOMAD evaluated the output and updated the input (*i.e.*, ρ and h_2) at each iteration. Algorithm 2 presents the simulation procedure for the homogenized FO under the pressure distribution of the flat foot. Algorithm 3 presents the optimization procedure by NOMAD.

The input geometrical variables were ρ and h_2. Moreover, the FO's domain was discretized into nine sub-domains (Figure 3). Each sub-domain represented a group of honeycomb cells having a height of $h_2^{(i)}$ and a relative density of $\rho^{(i)}$, where $i \in \{1, \ldots, 9\}$.

Constraints were mainly defined as the lower and upper bounds of the input variables (*i.e.*, $\mathbf{l_b} \leq \mathbf{x} \leq \mathbf{u_b}$) in the optimization problems. The relative density was limited to $10.0 \leq \rho \leq 80.0$ due to the manufactural limitations of 3D printing of honeycomb cells with a relative density of higher than 80% or lower than 10%. The constraint over the height of the cells was considered as $0.1 \leq h_2 \leq 5.0$ mm due to the limited space inside the shoes. Moreover, in one optimization problem, a group of nonlinear constraints was also defined

Algorithm 3: Optimization algorithm

Optimization parameters
`DIMENSIONS`: Number of variables.
$\mathbf{x_0}$: The initial point.
$\mathbf{l_b}, \mathbf{u_b}$: The bounds ($\mathbf{l_b} \leq \mathbf{x} \leq \mathbf{u_b}$).
$\mathrm{N_{Eval}}$: Maximum number of black-box evaluations.
Δ^m_0: Initial value of the mesh size to discretize the domain.
$\Delta^m_{\min}$: Minimum value of the mesh size to discretize the domain.
$\Delta^p_{\min}$: Minimum value of the poll size to create a frame.
Run NOMAD
$k \leftarrow 0$
for $i \in [\![1, N_{Eval}]\!]$ **do**
    $\Delta^m_{k+1} \leftarrow \Delta^m_k$ Update the mesh size
    $\Delta^p_{k+1} \leftarrow \Delta^p_k$ Update the poll size
    $\mathbf{x}_{k+1} \leftarrow \mathbf{x}_k$ Update the input
    Run Abaqus
    Evaluate the output $f(\mathbf{x}_{k+1})$
    if $\Delta^m_{k+1} \leq \Delta^m_{\min}$ *or* $\Delta^p_{k+1} \leq \Delta^p_{\min}$ **then**
        stop
Return optimal solution $\mathbf{x}^*$

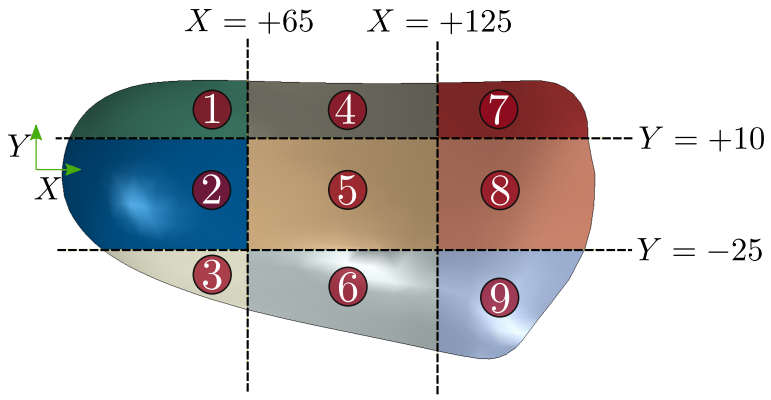

Figure 3: The discretized FO's domain to build a functionally graded honeycomb lattice structure (dimensions are in mm); Two vertical lines (with coordinates of $X = 65.0$ and $X = 125.0$) and two horizontal lines (with coordinates of $Y = -25$ and $Y = 10$) were considered to discretize the FO's domain into nine sub-domains. Each sub-domain includes a group of honeycomb cells having a relative density of $\rho^{(i)}$ and a height of $h_2^{(i)}$, where $i \in \{1, \ldots, 9\}$. In the optimization process, the effective properties of each group were computed using the continuous regression function resulting from the numerical homogenization process and assigned into the corresponding elements in the FE simulation. The optimization solver updates $\rho^{(i)}$ and/or $h_2^{(i)}$ in each iteration to minimize the given cost function(s).

such that the difference between the height of a sub-domain ($h_2^{(i)}$) against the neighbor sub-domains did not become higher than a given value δ_i. Such constraints were devised to yield a smoother surface at the optimal solution. Table 1 indicates the constraints over the variable h_2 and Figure 4 shows why imposing these constraints might be needed within the optimization process. Note that in NOMAD, the constraints were handled using the *Extreme Barrier* approach as per [18]:

$$f_\Omega := \begin{cases} f(x) & \text{if} \quad x \in \Omega \\ +\infty & \text{if} \quad x \notin \Omega \end{cases} \tag{2}$$

where Ω is the feasible domain of the variable x. Therefore, those trial points that are not in the feasible domain, would not be definitely selected as the optimal solution of the cost function $f(x)$.

Table 1: The constraints over the heights of the cells

$\delta_1 = \frac{1}{3}\left(\sum_i \left(h_2^{(1)} - h_2^{(i)}\right)^2\right)^{1/2}$	$i \in \{2,4,5\}$
$\delta_2 = \frac{1}{5}\left(\sum_i \left(h_2^{(2)} - h_2^{(i)}\right)^2\right)^{1/2}$	$i \in \{1,3,4,5,6\}$
$\delta_3 = \frac{1}{3}\left(\sum_i \left(h_2^{(3)} - h_2^{(i)}\right)^2\right)^{1/2}$	$i \in \{2,5,6\}$
$\delta_4 = \frac{1}{5}\left(\sum_i \left(h_2^{(4)} - h_2^{(i)}\right)^2\right)^{1/2}$	$i \in \{1,2,5,7,8\}$
$\delta_5 = \frac{1}{8}\left(\sum_i \left(h_2^{(5)} - h_2^{(i)}\right)^2\right)^{1/2}$	$i \in \{1,2,3,4,6,7,8,9\}$
$\delta_6 = \frac{1}{5}\left(\sum_i \left(h_2^{(6)} - h_2^{(i)}\right)^2\right)^{1/2}$	$i \in \{2,3,5,8,9\}$
$\delta_7 = \frac{1}{3}\left(\sum_i \left(h_2^{(7)} - h_2^{(i)}\right)^2\right)^{1/2}$	$i \in \{4,5,8\}$
$\delta_8 = \frac{1}{5}\left(\sum_i \left(h_2^{(8)} - h_2^{(i)}\right)^2\right)^{1/2}$	$i \in \{4,5,6,7,9\}$
$\delta_9 = \frac{1}{3}\left(\sum_i \left(h_2^{(9)} - h_2^{(i)}\right)^2\right)^{1/2}$	$i \in \{5,6,8\}$
$\delta_i \leq 4.0$	$i \in \{1,2,3,4,5,6,7,8,9\}$

The cost function was defined as a function of the predicted displacement field. The objective was to minimize the difference between the predicted out-of-plane displacement

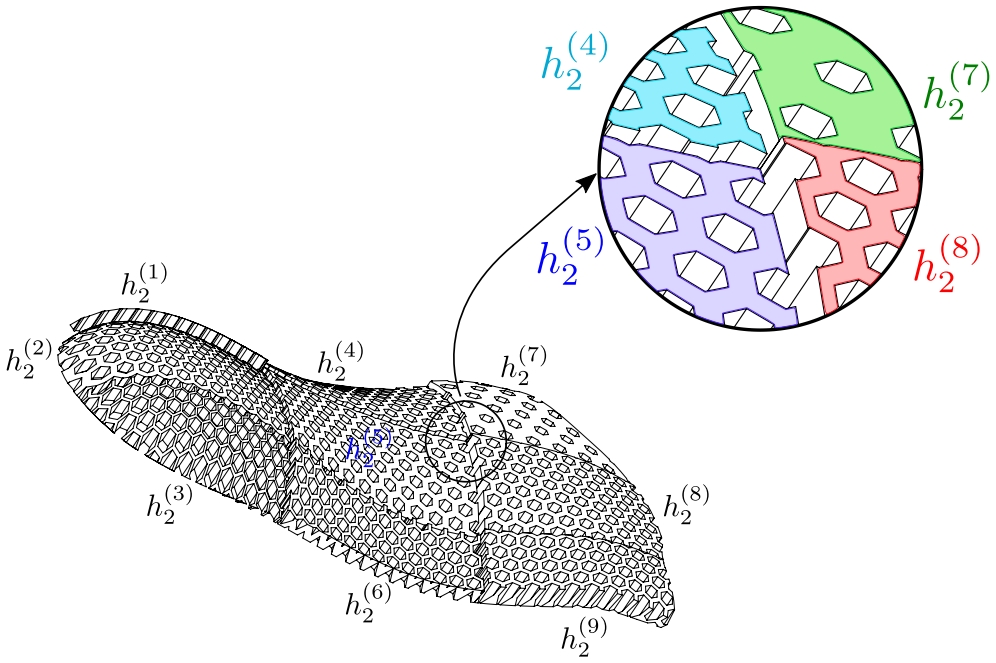

Figure 4: Variation of the height of the honeycomb cells in the discretized nine sub-domains of the FO. This figure schematically shows that it might be necessary to impose a set of constraints over the height of the cells to limit abrupt changes. The necessity comes from an undesirable large difference between the height of the cells in the adjacent sub-domains which might make the manufacturing process difficult and also cause a high stress concentration. To mitigate this issue, we proposed imposing a group of non-linear constraints over the height of the cells that are presented in Table 1 to provide a smoother surface at the optimal solution.

field (U_Z) by the current FE model against the predicted displacement field by the reference FE model (U_Z^{R}) of a FO having arbitrary geometrical parameters ($\mathbf{x}^{\mathrm{R}}$). Therefore, in this way, the expected minimum value was $f(\mathbf{x}^{\mathrm{R}}) = 0.0$. The absolute error of the resulting optimal solution ($\mathbf{x}^*$) was estimated as per:

$$\mathbf{e} = |\mathbf{x}^{\mathrm{R}} - \mathbf{x}^*|. \tag{3}$$

The optimization process was stopped when it reached the given stopping criteria. Three stopping criteria were tested including; the maximum number of black-box evaluations ($\mathrm{N_{Eval}}$), the minimum value of the mesh size (Δ^m_{min}) and the minimum value of the poll size (Δ^p_{min}). It was considered that $\Delta^p_{\mathrm{min}} = \sqrt{\Delta^m_{\mathrm{min}}}$ for $\Delta^m_{\mathrm{min}}, \Delta^p_{\mathrm{min}} < 1$ [18]. Note that the

initial mesh size (Δ_0^m) can be also determined. The above hyperparameters were defined in NOMAD for each optimization example.

2.6 Optimization examples

2.6.1 Single-variable optimization examples

The single-variable optimization consisted in optimizing either ρ or h_2 uniformly distributed through the whole FO. In this regard, the first example was:

$$\begin{aligned} \min_{x \in R} \quad & ||U_Z - U_Z^{\mathrm{R}}||_2 \\ \text{s.t.} \quad & 10.0 \leq x \leq 80.0, \end{aligned} \tag{4}$$

while the height of the cells was set at $h_2 = 3.0\,\mathrm{mm}$. The target displacement field was predicted by a honeycomb homogenized model having a relative density of $\rho = 40\%$. The expected optimal solution was therefore $x^{\mathrm{R}} = 40\%$. Two initial solutions were considered as $x_0 = 10\%$ and $x_0 = 80\%$ to start the optimization. The initial mesh size was $\Delta_0^m = 10.0$. Moreover, the stopping criteria was set to $\Delta_{\min}^m = 0.25$ and $\Delta_{\min}^p = 0.5$.

The second example was:

$$\begin{aligned} \min_{x \in R} \quad & ||U_Z - U_Z^{\mathrm{R}}||_2 \\ \text{s.t.} \quad & 0.1 \leq x \leq 5.0, \end{aligned} \tag{5}$$

while the relative density was $\rho = 40\%$. The reference solution was $x^{\mathrm{R}} = 3.0\,\mathrm{mm}$. Two initial points were considered as $x_0 = 0.1\,\mathrm{mm}$ and $x_0 = 5.0\,\mathrm{mm}$. The hyper parameters were considered as $\Delta_0^m = 1.0$, $\Delta_{\min}^m = 0.01$ and $\Delta_{\min}^p = 0.1$.

2.6.2 Multi-variables optimization examples

The third example was a multi-variable optimization of $\rho^{(i)}$, as per:

$$\begin{aligned} \min_{\mathbf{x}\in R^9} \quad & ||U_Z - U_Z^{\mathrm{R}}||_2 \\ \mathbf{x} = \quad & [\rho^{(1)}, \rho^{(2)}, \ldots, \rho^{(9)}]^{\mathrm{T}} \\ \text{s.t.} \quad & 10.0 \leq \rho^{(i)} \leq 80.0 \\ & i \in \{1, 2, \ldots, 9\}, \end{aligned} \tag{6}$$

while all $h_2^{(i)}$ were set to $h_2^{(i)} = 3.0\,\mathrm{mm}$. To start the optimization, the initial solution was set to $\rho^{(i)} = 10\%$ for all sub-domains. Moreover, the initial mesh size and the stopping criteria were set to $\Delta_0^m = 10.0$, $\Delta_{\min}^m = 0.25$ and $\Delta_{\min}^p = 0.5$. The reference solution of this example was:

$$\mathbf{x}^{\mathrm{R}} = [30.0, 35.0, 40.0, 45.0, 50.0, 55.0, 60.0, 65.0, 70.0]^{\mathrm{T}}\%. \tag{7}$$

The fourth example was an optimization of $h_2^{(i)}$, as per:

$$\begin{aligned} \min_{\mathbf{x}\in R^9} \quad & ||U_Z - U_Z^{\mathrm{R}}||_2 \\ \mathbf{x} = \quad & [h_2^{(1)}, h_2^{(2)}, \ldots, h_2^{(9)}] \\ \text{s.t.} \quad & 0.1 \leq h_2^{(i)} \leq 5.0 \\ & i \in \{1, 2, \ldots, 9\}, \end{aligned} \tag{8}$$

while all $\rho^{(i)}$ were set to $\rho^{(i)} = 40.0\%$. The initial solution was set to $h_2^{(i)} = 0.1$ for all sub-domains. The hyper parameters were $\Delta_0^m = 1.0$, $\Delta_{\min}^m = 0.01$ and $\Delta_{\min}^p = 0.1$. The reference solution was:

$$\mathbf{x}^{\mathrm{R}} = [1.0, 1.5, 2.0, 2.5, 3.0, 3.5, 4.0, 4.5, 5.0]^{\mathrm{T}}\mathrm{mm}. \tag{9}$$

The fifth example was an optimization of $\rho^{(i)}$ and $h_2^{(i)}$, simultaneously, as per:

$$\begin{aligned} \min_{\mathbf{x}\in R^{18}} \quad & ||U_Z - U_Z^{\mathrm{R}}||_2 \\ & \mathbf{x} = [\rho^{(1)}, \ldots, \rho^{(9)}, h_2^{(1)}, \ldots, h_2^{(9)}]^{\mathrm{T}} \\ \text{s.t.} \quad & 10.0 \leq \rho^{(i)} \leq 80.0 \\ & 0.1 \leq h_2^{(i)} \leq 5.0 \\ & i \in \{1, 2, \ldots, 9\}. \end{aligned} \tag{10}$$

The reference solution was:

$$\mathbf{x}^{\mathrm{R}} = [30, 35, 40, 45, 50, 55, 60, 65, 70, 1.0, 1.5, 2.0, 2.5, 3.0, 3.5, 4.0, 4.5, 5.0]^{\mathrm{T}}\%, \mathrm{mm}. \tag{11}$$

The initial solutions were considered as $\rho^{(i)} = 10\%$ and $h_2^{(i)} = 0.1$ for all sub-domains. The initial mesh size and the stopping criteria for the relative density were $\Delta_0^m = 10.0$, $\Delta_{\min}^m = 0.25$, $\Delta_{\min}^p = 0.5$ and for the height of the cells were $\Delta_0^m = 1.0$, $\Delta_{\min}^m = 0.01$ and $\Delta_{\min}^p = 0.1$. Moreover, the computational budget was set to $\mathrm{N_{Eval}} = 2000$.

2.6.3 Multi-variable and bi-objective optimization example

The sixth example was an optimization of $h_2^{(i)}$ and $\rho^{(i)}$ featuring two cost functions to achieve the target displacement as well as minimizing the total mass, as per:

$$\begin{aligned} \min_{\mathbf{x}\in R^{18}} \quad & F(\mathbf{x}) = \Big(f^{(1)}(\mathbf{x}), f^{(2)}(\mathbf{x})\Big) \\ & f^{(1)} = ||U_Z - U_Z^{\mathrm{R}}||_2 \\ & f^{(2)} = \left(\frac{1}{\sum_i a^{(i)}}\right) \sum_i \rho^{(i)} h_2^{(i)} a^{(i)} \\ & \mathbf{x} = [\rho^{(1)}, \ldots, \rho^{(9)}, h_2^{(1)}, \ldots, h_2^{(9)}]^{\mathrm{T}} \\ \text{s.t.} \quad & 0.1 \leq h_2^{(i)} \leq 5.0 \\ & 10.0 \leq \rho^{(i)} \leq 80.0 \\ & \delta_i - 4.0 \leq 0.0 \\ & i \in \{1, 2, \ldots, 9\}. \end{aligned} \tag{12}$$

In the first objective, U_Z^{R} was the predicted displacement field by a homogenized model consisting of the reference geometrical parameters like the previous example (Equation 11). The second objective represents the apparent total mass of the FO, in which $\mathbf{a}$ was a constant vector consisting of the area of each sub-domain:

$$\mathbf{a} = [676, 2214, 1177, 1685, 2173, 1155, 1238, 1753, 865]^{\mathrm{T}} \quad \mathrm{mm}^2. \tag{13}$$

The computational budget was set to $\mathrm{N_{Eval}} = 1000$. The initial solution and other hyperparameters (*i.e.,* $\mathbf{x_0}$, Δ_0^m, $\Delta_{\min}^m$, $\Delta_{\min}^p$) were considered similar to Example #5. Moreover, the nonlinear group of constraints (Table 1) were also imposed to the variables $h_2^{(i)}$. Note that there is no unique optimal solution in this example and the final response is a set of optimal solutions (so called *Pareto front* [18]).

3 Results

3.1 Computed effective properties of honeycomb cells

Figure 5 shows the computed effective properties of the honeycomb cells having relative densities of $\rho = 10\% - 80\%$ with 10% increments, as well as the regression results using polynomial regression functions. Except for the Poisson's ratios, the other computed effective elastic constants are normalized with the bulk properties E_s and G_s. Moreover, the computed regression coefficients are reported in Table 2.

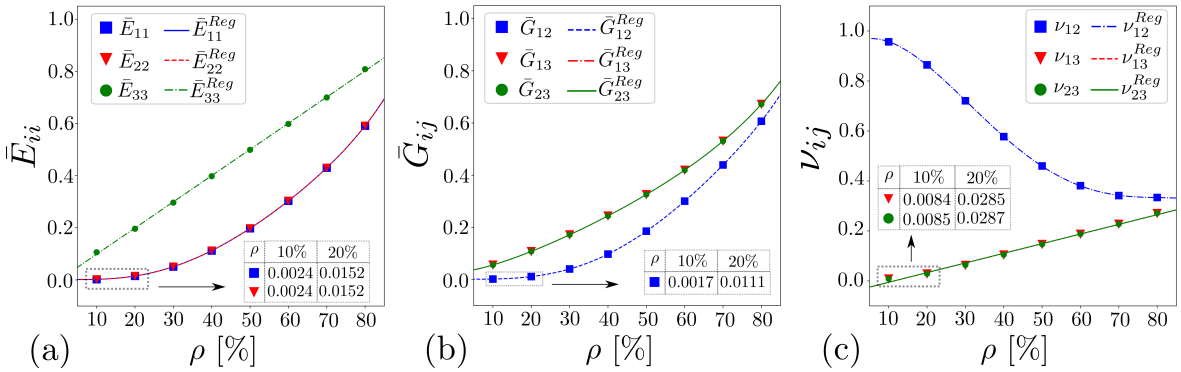

Figure 5: Computed effective properties of the honeycomb cells; (a) axial elastic constants $\bar{E}_{ii}$, (b) shear elastic constants $\bar{G}_{ij}$ and (c) Poisson's ratios $\bar{\nu}_{ij}$. The figure also shows the continuous regression functions using a polynomial regression function.

Table 2: Regression of the computed effective proprieties using $R(\rho) = \sum_{i=0}^{6} \Theta_i \rho^i$.

Property	Θ_0	Θ_1	Θ_2	Θ_3	Θ_4	Θ_5	Θ_6
$\bar{E}_{11}$	0.0	0.0	0.0	3.57e-06	-2.38e-05	-6.93e-05	2.20e-03
$\bar{E}_{22}$	0.0	0.0	0.0	2.23e-06	1.05e-05	-4.92e-04	4.10e-03
$\bar{E}_{33}$	1.00e-02	-1.82e-03	-	-	-	-	-
$\bar{G}_{12}$	0.0	0.0	0.0	-1.71e-06	5.31e-05	-6.07e-04	3.23e-03
$\bar{G}_{13}$	0.0	0.0	0.0	-6.01e-06	2.39e-04	9.85e-04	2.72e-02
$\bar{G}_{23}$	0.0	0.0	0.0	-4.91e-06	2.08e-04	1.38e-03	2.53e-02
ν_{12}	0.0	1.29e-05	-8.63e-04	8.28e-03	9.48e-01	-	-
ν_{13}	3.86e-03	-4.43e-02	-	-	-	-	-
ν_{23}	3.86e-03	-4.39e-02	-	-	-	-	-

3.2 Optimization results

In the single-variable optimization examples, the solver found the exact solutions in less than 8 minutes. Figure 6 shows the variation of the input and output with respect to the number of evaluations in Example #1. The solver was stopped by reaching to the predefined minimum mesh size. The minimum values were found at the third and seventh evaluations, while the solver was stopped at the seventh and eighth evaluations for the initial points of $x_0 = 10$ and $x_0 = 80$, respectively. For both initial points, the optimal solution was $x^* = 40.0\%$ and where $f(x^*) = 0.0$. The error of the optimal solution was therefore $e = 0.0$. Similarly, the optimal results of Example #2 (Figure 7), for both given initial points, were $x^* = 3.0\%$ and $f(x^*) = 0.0$, which returned $e = 0.0$. In this example, the solver found the optimal solutions after 4 and 11 evaluations, while it was stopped at 23 and 17 since it reached the minimum mesh size for the initial points of $x_0 = 0.1$ and $x_0 = 5.0$, respectively. These two single-variable optimization examples were the easiest cases in which the solver rapidly found the exact solution.

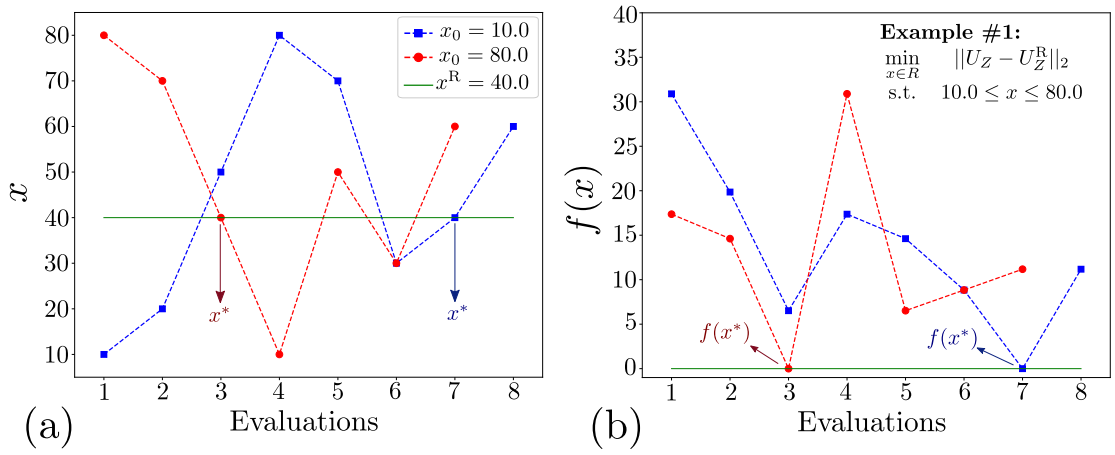

Figure 6: Variations of (a) x and (b) $f(x)$ with respect to the number of evaluations in optimization Example #1, in which the single variable was relative density ρ and the objective was to minimize $||U_Z - U_Z^R||_2$. In this example, the hyper parameters were set to $\Delta_0^m = 10.0$, $\Delta_{\min}^m = 0.25$ and $\Delta_{\min}^p = 0.5$. Two initial points were considered as $x_0 = 10$ and $x_0 = 80$ in which the solver reached the minimum mesh size after 8 and 7 evaluations, respectively. In both cases, the optimal solutions are exactly equal to the reference solution.

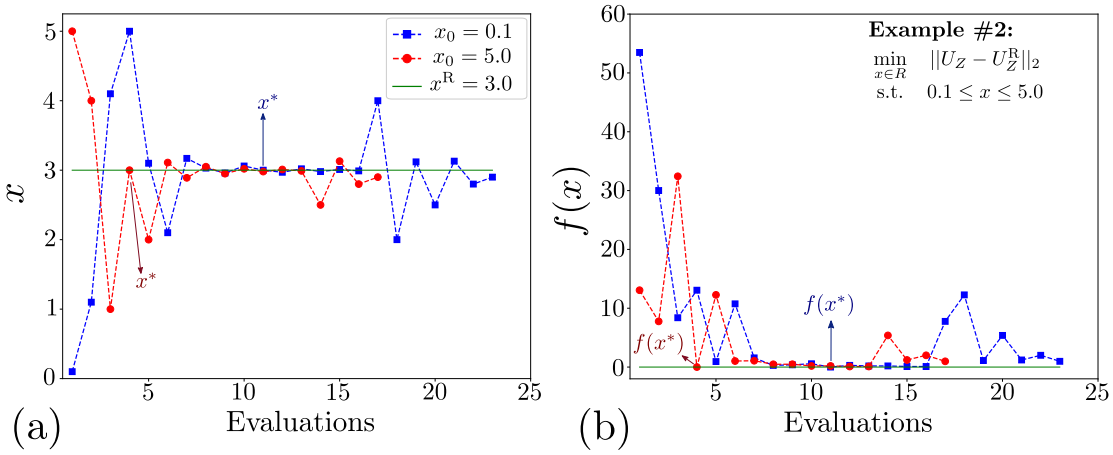

Figure 7: Variations of (a) x and (b) $f(x)$ with respect to the number of evaluations in optimization Example #2, in which of the single variable was the height of the cells and the objective was to minimize $||U_Z - U_Z^{\mathrm{R}}||_2$. In this example, the hyper parameters were set to $\Delta_0^m = 1.0$, $\Delta_{\min}^m = 0.01$ and $\Delta_{\min}^p = 0.1$. Two initial points were considered as $x_0 = 0.1$ and $x_0 = 5.0$ in which the solver reached the minimum mesh size after 23 and 17 evaluations, respectively. In both cases, the optimal solutions are exactly equal to the reference solution.

In the multi-variable optimization of Example #3, after 2 hours and 20 minutes (440 evaluations), the solver reached the minimum mesh size and resulted in $f(\mathbf{x}^*) = 0.31$ (Figure 8). The maximum absolute difference between the optimal solution and the reference solution was 10%. In Example #4, after 2 hours and 48 minutes (526 evaluations) the solver reached the minimum mesh size and the cost function was minimized to $f(\mathbf{x}^*) = 0.11$ (Figure 9). In this case, the maximum absolute difference between the optimal solution and the reference solution was 0.98 mm. In Example #5, having 18 variables (Figure 10) and after almost 10 hours, the solver reached the maximum budget (2000 evaluations) and the cost function was minimized to $f(\mathbf{x}^*) = 0.19$. Table 3 reports the effective properties resulted from the optimized relative densities. Figure 11 shows the reference solution, the optimal solution and their absolute difference for Example #5. In this example, the maximum absolute differences between the reference solution and the optimal solution were 18.93% and 2.24 mm for $\rho^{(3)}$ and $h_2^{(3)}$, respectively (Figure 11). The results of Examples #3, #4 and #5 imply that, in high dimensional optimization problems, the solver may find a different optimal

Table 3: The effective properties of the sub-domains in Example #5.

Properties	S.1	S.2	S.3	S.4	S.5	S.6	S.7	S.8	S.9
E_{11} [MPa]	101	447	37	257	640	583	353	528	1166
E_{22} [MPa]	102	448	37	258	641	584	353	529	1166
E_{33} [MPa]	609	1070	453	857	1250	1200	941	1149	1621
G_{12} [MPa]	29	155	10	83	232	209	118	187	437
G_{13} [MPa]	127	258	86	193	320	303	226	284	489
G_{23} [MPa]	127	258	86	193	320	302	226	284	489
ν_{12}	0.72	0.43	0.84	0.55	0.37	0.39	0.48	0.40	0.33
ν_{13}	0.07	0.15	0.03	0.11	0.19	0.18	0.13	0.17	0.25
ν_{23}	0.07	0.15	0.03	0.11	0.19	0.18	0.13	0.17	0.26

solution when compared to the reference solution, while the minimized cost function is still acceptable. By acceptable we mean a minimized cost functions smaller than 0.5 mm. We accepted this value since the resulting displacement field from the optimized FO would be very close to the target displacement. The maximum absolute differences between the reference displacement and the displacement from the optimized FO (*i.e.*, $\max(|U_Z^{\mathrm{R}} - U_Z^*|)$) were 0.06 mm, 0.01 mm and 0.04 mm for Examples #3, #4 and #5, respectively. Note that literature shows that the maximum out-of-plane displacement of FOs may reach 10.0 mm during walking [29]. Considering this range and the computed errors, all of these three multi-variable optimization examples were successfully solved.

In the bi-objective optimization of Example #6 (Figure 12a), the Pareto front was found after 5 hours (1000 evaluations) to minimize the apparent total mass and to reach the target deflection. Since these objectives are conflicting, there is no single vector $\mathbf{x}^*$ that minimizes both of them, simultaneously. In this case, the decision maker should select the best answer among the optimal solutions considering the intended application. One possible solution, for instance, could be $(f^{(1)}, f^{(2)}) = (5.06, 91.59)$. In the optimized solution of the single objective optimization Example #5, the optimized stiffness returned $f^{(1)} = 0.19$, while the apparent mass was 159.34. Solving the bi-objective optimization of Example #6 reduced the apparent mass by about 42%. Although the cost function related to the stiffness is increased from 0.19 mm to 5.06 mm, controlling the FO's mass might be also important since heavy FOs may

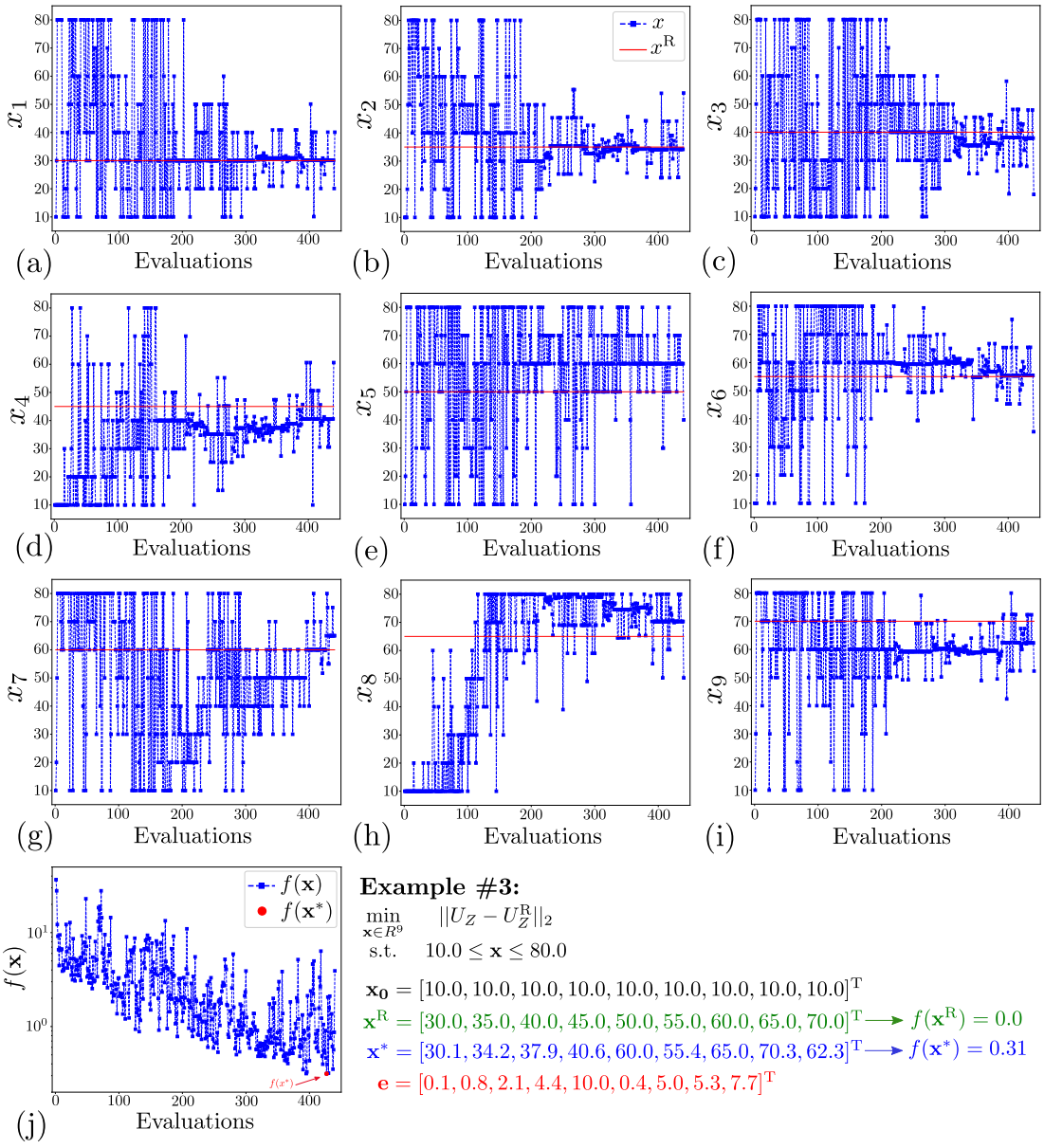

Figure 8: Variations of (a-i) x_i and (j) $f(\mathbf{x})$ in a log scale and with respect to the number of evaluations in optimization Example #3, in which the variables were the relative densities of the cells at nine sub-domains and the objective was to minimize $||U_Z - U_Z^{\mathrm{R}}||_2$. In this example, the hyper parameters were set to $\Delta_0^m = 10.0$, $\Delta_{\min}^m = 0.25$ and $\Delta_{\min}^p = 0.5$. The initial point was considered as $x_i = 10.0$. The solver reached the minimum mesh size after 440 evaluations. The optimal solution has a maximum absolute error of 10.0% in sub-domain 5 and the cost function was minimized to $f(\mathbf{x}^*) = 0.31$.

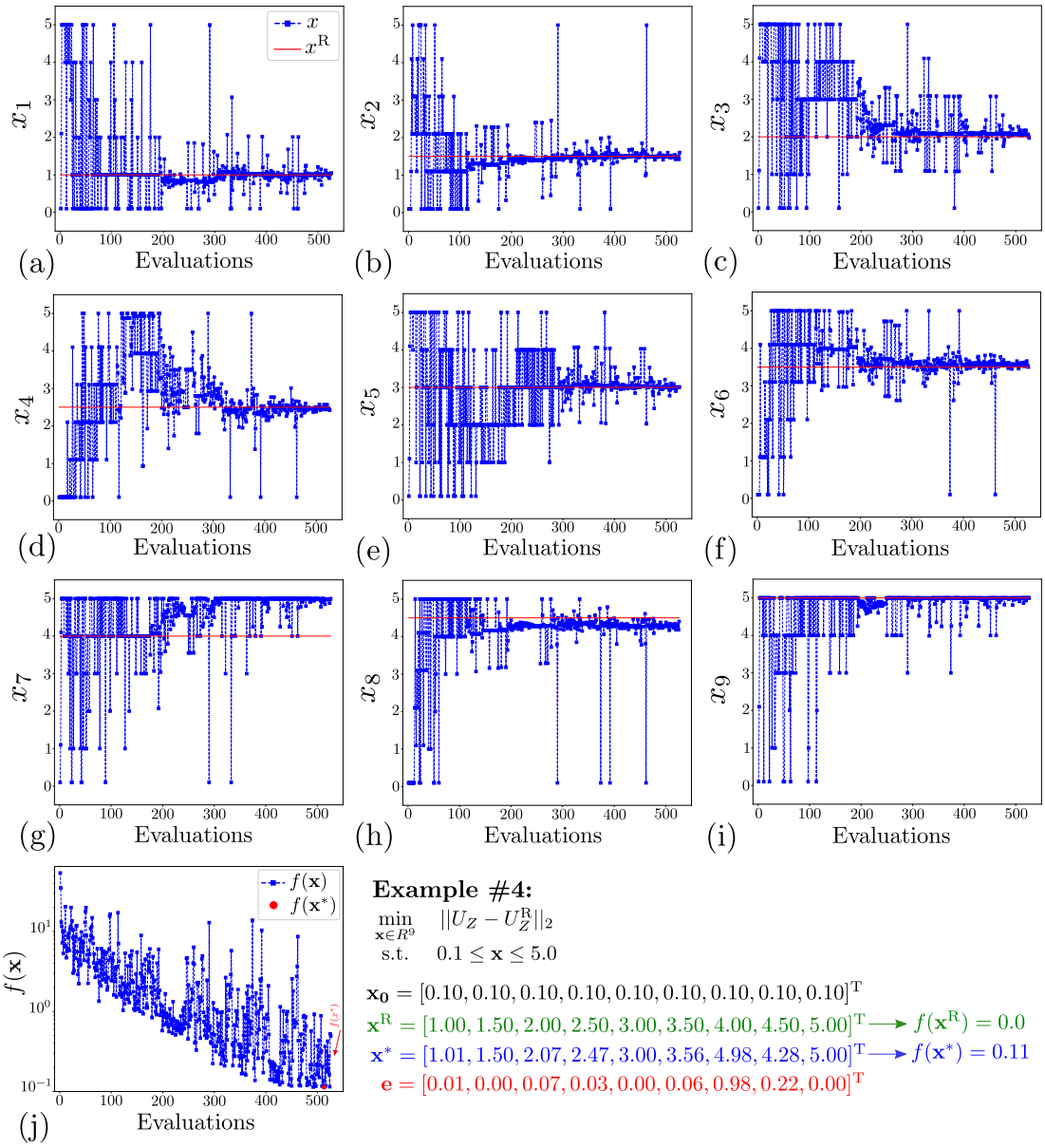

Figure 9: Variations of (a-i) x_i and (j) $f(\mathbf{x})$ in a log scale and with respect to the number of evaluations in optimization Example #4, in which the variables were the heights of the cells at nine sub-domains and the objective was the minimization of $||U_Z - U_Z^{\mathrm{R}}||_2$. In this example, the hyper parameters were set to $\Delta_0^m = 1.0$, $\Delta_{\min}^m = 0.01$ and $\Delta_{\min}^p = 0.1$. The initial point was considered as $x_i = 0.1$. The solver reached the minimum mesh size after 526 evaluations. The optimal solution has a maximum absolute error of 0.98 mm in sub-domain 7 and the cost function was minimized to $f(\mathbf{x}^*) = 0.11$.

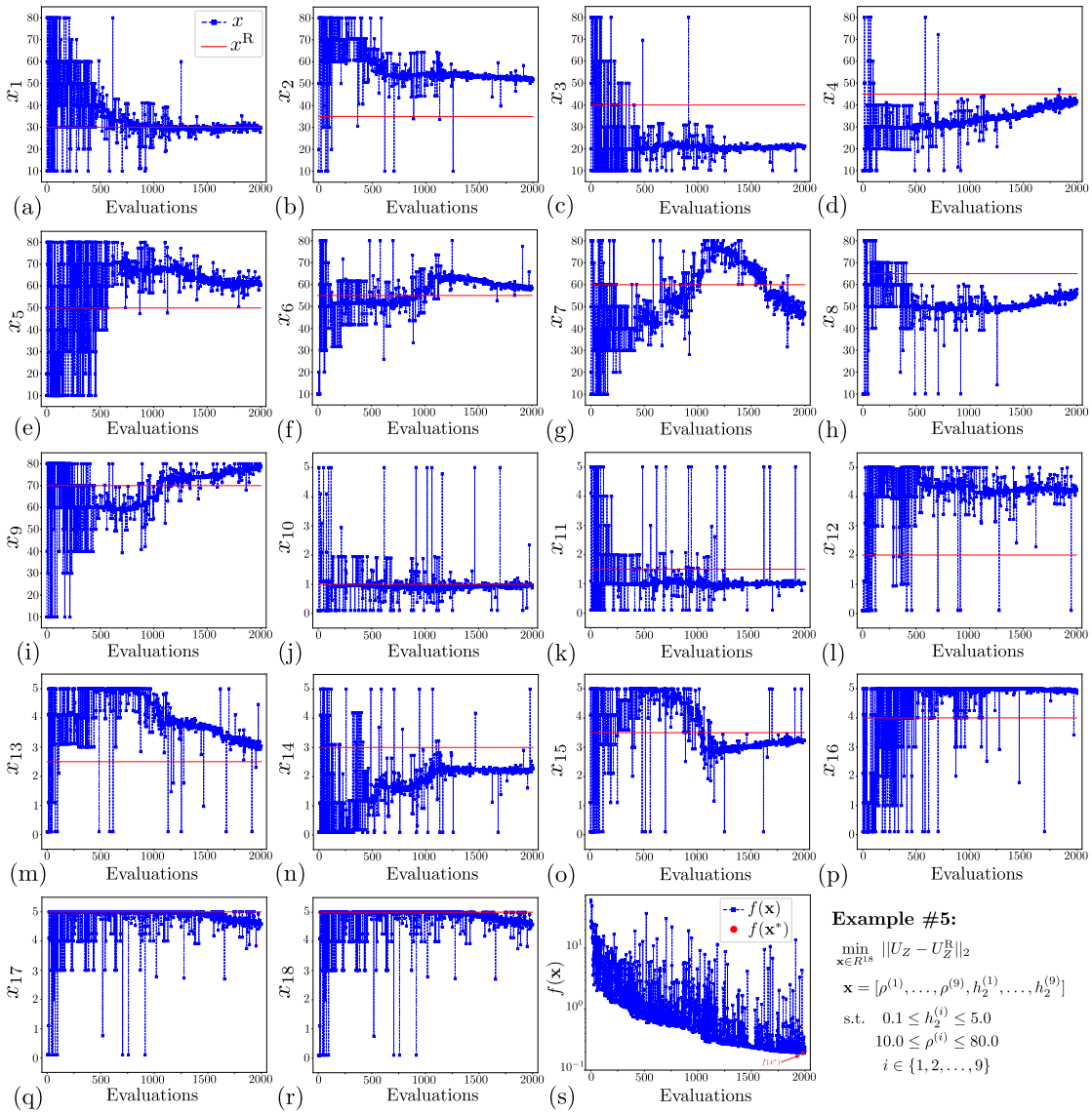

Figure 10: Variations of (a-r) x_i and (s) $f(\mathbf{x})$ in a log scale and with respect to the number of evaluations in optimization Example #5, in which the multiple variables were the relative densities of the cells (*i.e.*, x_i for $i \in \{1, \ldots, 9\}$) and the heights of the cells (*i.e.*, x_i for $i \in \{10, \ldots, 18\}$) at nine sub-domains and the objective was to minimize $||U_Z - U_Z^{\mathrm{R}}||_2$; In this example, the budget was set to $\mathrm{N_{Eval}} = 2000$. The initial point was considered as $x_i = 10.0$ for $i \in \{1, \ldots, 9\}$ and $x_i = 0.1$ for $i \in \{10, \ldots, 18\}$. The maximum absolute difference between the reference solution and the optimal solution is 18.93% and 2.24 mm for $\rho^{(3)}$ and $h_2^{(3)}$, respectively. Yet, the cost function was minimized to $f(\mathbf{x}^*) = 0.19$.

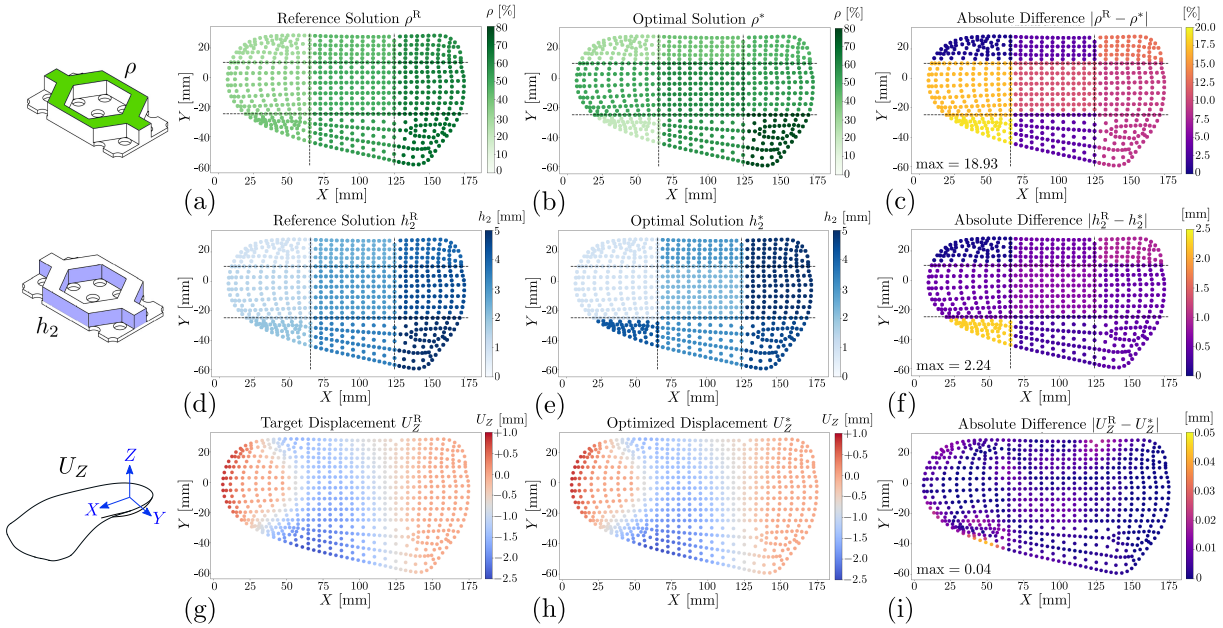

Figure 11: Optimized solution and the resulting displacement field in Example #5; (a) ρ^{R}, (b) ρ^*, (c) $|\rho^* - \rho^{\mathrm{R}}|$, (d) h_2^{R}, (e) h_2^*, (f) $|h_2^* - h_2^{\mathrm{R}}|$, (g) U_Z^{R}, (h) U_Z^* and (i) $|U_Z^* - U_Z^{\mathrm{R}}|$. The maximum absolute difference between the reference relative density and the optimized one is 18.93% and for the reference height of the cells and the optimized one it is 2.24 mm. In both cases, the maximum error is for sub-domain 3. Nevertheless, the resulting displacement field from the optimized FO is very close to the target displacement field having a maximum absolute difference of 0.04 mm. This implies that the target displacement might be satisfactorily achieved with a different set of solutions than the reference solution.

increase the energy consumption and it may cause fatigue during walking or running [32]. Furthermore, minimizing the FO's mass reduces the material consumption and leads to a more economical fabrication of 3D printed FOs. Note that the mass could be also considered as a constraint or a regularization term in the cost function instead of adding it in the second objective function in the optimization problem. Figure 12b shows that, at every iteration, the imposed nonlinear constraints were satisfied.

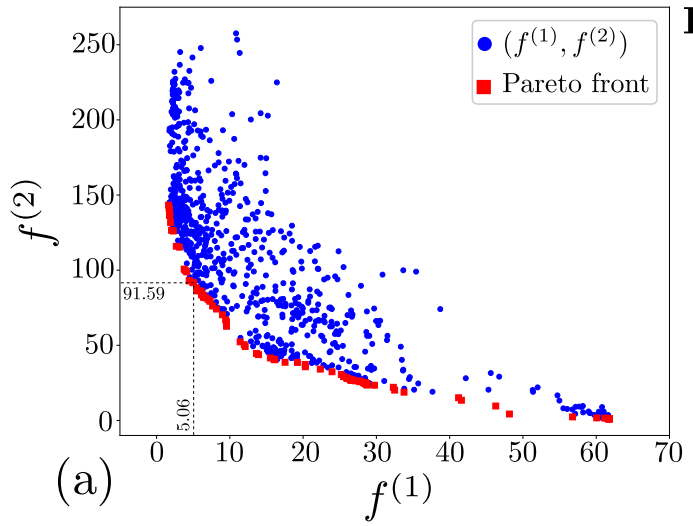

Example #6:

$$\min_{\mathbf{x}\in R^{18}} \quad F(\mathbf{x}) = \left(f^{(1)}(\mathbf{x}), f^{(2)}(\mathbf{x})\right)$$

$$f^{(1)} = ||U_Z - U_Z^{\mathrm{R}}||_2$$

$$f^{(2)} = \frac{1}{\sum_i a^{(i)}} \sum_i \rho^{(i)} h_2^{(i)} a^{(i)}$$

$$\mathbf{x} = [\rho^{(1)}, \ldots, \rho^{(9)}, h_2^{(1)}, \ldots, h_2^{(9)}]^{\mathrm{T}}$$

$$\text{s.t.} \quad 0.1 \leq h_2^{(i)} \leq 5.0$$

$$10.0 \leq \rho^{(i)} \leq 80.0$$

$$\delta_i - 4.0 \leq 0.0$$

$$i \in \{1, 2, \ldots, 9\}$$

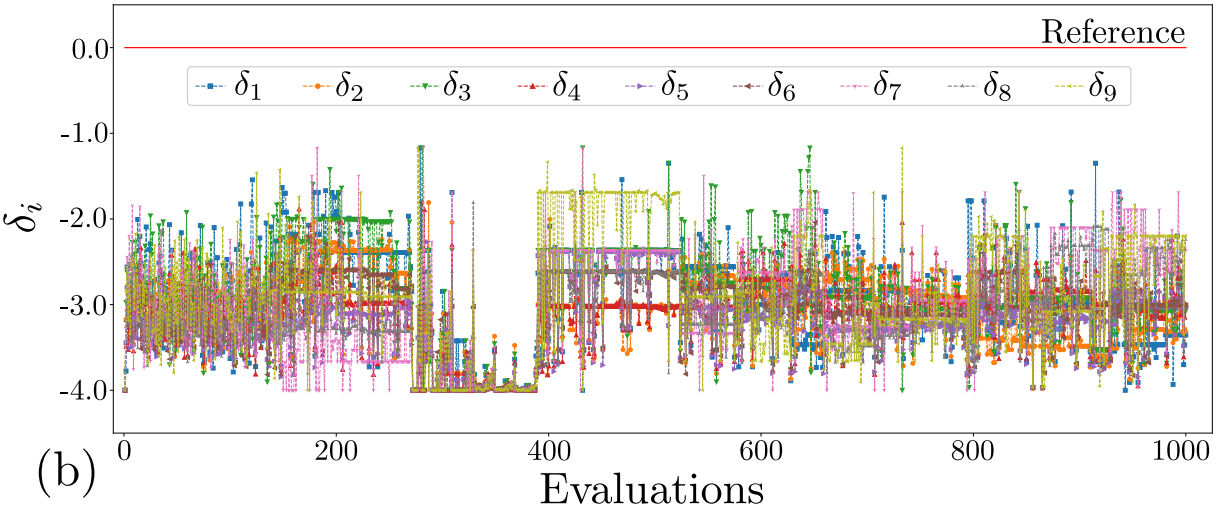

Figure 12: Results of Example #6: Optimization of $\rho^{(i)}$ and $h_2^{(i)}$ when there were two objectives including the minimization of $f^{(1)} = ||U_Z - U_Z^{\mathrm{R}}||_2$ and $f^{(2)} = \frac{1}{\sum a^{(i)}} \sum \rho^{(i)} h_2^{(i)} a^{(i)}$ where $i \in \{1, \ldots, 9\}$. a) The evaluated cost functions and the Pareto front, b) values of nine constraints versus the number of evaluations. Figure (a) shows a set of possible solutions which leads to minimize both cost functions. The first cost function is linked to the structure's stiffness and the second one is linked to the structure's total mass. Based on the user's preference, the best solution might be selected among the optimal solutions. For instance, one possible solution could be $(f^{(1)}, f^{(2)}) = (5.06, 91.59)$. Figure (b) shows that the imposed non-linear constraints in the problem have been satisfied for every evaluation. The Extreme barrier technique was an efficient technique to filter the solutions.

4 Discussion

4.1 Required computational time and memory

Running each FE simulation of the homogenized model approximately requires 19 seconds and its required memory is about 18 MB. A summary of the optimization parameters and the needed computational time for each example using the homogenized model are reported in Table 4. The explicit FE simulation of the optimized and modified FO, resulting from Example #5, takes 1 483 seconds in which the required memory is 3 715 MB. This means that the homogenized model is 78 times faster and 206 times more efficient than the explicit model in terms of the computational time and memory, respectively. Running 2000 times the explicit FE simulation in an optimization process would require 823 hours (34 days) when compared to 10 hours with the homogenized model. The presented surrogate optimization, therefore, accelerates the whole prescription time. For instance, the total estimated time from starting the clinical test to the manufacturing of the FOs using the presented surrogate is about 44 hours. This estimated time includes 1 hour to diagnose the target FO's deflection (*i.e.*, U_Z^{R}), 1 hour to measure the foot pressure (*i.e.*, $P(X, Y, Z)$), 2 hours for 3D scanning of the feet, 10 hours to optimize 18 variables and finally 30 hours for additive manufacturing of a pair of FOs (*e.g.*, using Fused Deposition Modeling 3D printing machine *Raise3D Pro2 Technologies, Inc., US* by *Polylactic acid* filament and 0.4 mm nozzle). The optimized 3D printed FO would be ready in less than two days.

4.2 Improving the results

From a biomechanical point of view, the cost function can be articulated to meet the therapeutic needs of a patient with flat feet. For instance, the cost function might be extracted from a normal foot. In this way, the target deflection at the medial longitudinal arch of the flat foot can be roughly determined according to the navicular drop test of a person with a normal foot having the same gender and foot length [33]. From an optimization point

Table 4: Computational time and optimization parameters of the examples.

Prob.	var.	obj.	$\mathbf{x_0}$	stopped by	#eval.	time$[h:m:s]$	$f(\mathbf{x}^*)$
Ex.#1	1	1	10	$\Delta^m_{\min}$	8	00 : 02 : 39	0.00
Ex.#1	1	1	80	$\Delta^m_{\min}$	7	00 : 02 : 17	0.00
Ex.#1	1	1	10	$\mathrm{N_{Eval}}$	50	00 : 16 : 01	0.00
Ex.#1	1	1	80	$\mathrm{N_{Eval}}$	50	00 : 15 : 56	0.00
Ex.#2	1	1	0.1	$\Delta^m_{\min}$	23	00 : 07 : 22	0.00
Ex.#2	1	1	5.0	$\Delta^m_{\min}$	17	00 : 05 : 19	0.00
Ex.#2	1	1	0.1	$\mathrm{N_{Eval}}$	50	00 : 15 : 48	0.00
Ex.#2	1	1	5.0	$\mathrm{N_{Eval}}$	50	00 : 15 : 57	0.00
Ex.#3	9	1	[10]	$\Delta^m_{\min}$	440	02 : 19 : 53	0.31
Ex.#3	9	1	[10]	$\mathrm{N_{Eval}}$	1000	05 : 16 : 35	0.08
Ex.#4	9	1	[0.1]	$\Delta^m_{\min}$	526	02 : 48 : 06	0.11
Ex.#4	9	1	[0.1]	$\mathrm{N_{Eval}}$	1000	05 : 09 : 21	0.04
Ex.#5	18	1	[10, 0.1]	$\mathrm{N_{Eval}}$	2000	09 : 54 : 26	0.19
Ex.#6	18	2	[10, 0.1]	$\mathrm{N_{Eval}}$	1000	04 : 56 : 44	pareto
Ex.#6	18	2	[10, 0.1]	$\mathrm{N_{Eval}}$	8000	46 : 30 : 03	pareto

of view, there are four ways to reduce the required number of evaluations and get a faster response: 1) reducing the number of variables (using model order reduction techniques such as principal component analysis [34]); 2) reducing the intervals of the variables ρ and h_2 by modifying the lower and upper bounds based on the orthotics experience with the product; 3) improving the initial solution (using the educated guesses); 4) increasing the minimum mesh size $\Delta^m_{\min}$ and/or the minimum poll size $\Delta^p_{\min}$ in the stopping criteria. On the other hand, removing the minimum mesh size and increasing the number of evaluations, increases the accuracy of the optimized solution (see for instance Appendix C). Conducting a sensitivity analysis highlights how to compromise between the accuracy and the computational cost. It also answers how a change in a variable affects the structural behavior of the FO and, thus, it helps to set the above hyper-parameters before starting the optimization process. Using other optimization solvers (such as genetic algorithm [35]) may also improve both the accuracy and the computational efficiency. From a manufacturing point of view, the 3D printing limitations (such as minimum wall thickness) can be imposed on the solution by setting the constraints over the geometrical parameters.

4.3 A qualitative comparison with related works

To the best of our knowledge, the presented framework was the first stiffness optimization of the honeycomb lattice FO for the flat foot condition. The previous optimized FOs were mostly related to diabetic feet [36, 37]. In the diabetic FOs, the objective is to minimize the predicted contact stress between the foot and the FO to mitigate the risk of feet ulcers [38]. Having a clinical-based objective function enables previous authors to fabricate their optimized FO and clinically evaluate its performance [36], which has not been done in this research. In designing a FO for the flat foot condition, further studies are required to mathematically express the expectations from an orthopedic FO for the flat foot deformity. From a mechanical and computational point of view, however, the presented homogenized FO is more comprehensive and more computationally efficient, when compared to the previous FE simulation-based optimization of FOs. It is more comprehensive because previous authors considered only an isotropic property for the FO's material in their FE simulations [36, 37]. In a functionally graded lattice FO, Tang et al. [36] did not implement the numerical homogenization over the cells and they employed one elastic constant as the effective property of the cells. It is more computationally efficient because the previous authors used 3D elements to mesh the FO, which of course increases the computational cost [36,37]. Moreover, Tang et al. [36] optimized the FO by the Grid Search (GS) algorithm, in which the variables are discretized and the cost function is evaluated at the points and the best solution is selected from the evaluated points. Although GS is not a heuristic method and consists of a convergence proof, it requires a tremendous number of evaluations to find a solution whose cost function is close to the optimal one [18].

4.4 Limitations and future works

The first limitation of this work is related to the applied pressure distribution over the FO. In fact, changing the FO's stiffness affects the interaction between the foot and the FO, and correspondingly alters the foot pressure distribution [39]. On other hand, we assumed that

the applied foot pressure remains constant during the whole optimization procedure. To solve this issue, measuring the foot pressure distribution for several FOs with different stiffness and conducting a regression may provide a continuous regression function of pressure with respect to the FO's stiffness. This task could be also done by a verified and validated foot/FO/ground FE simulation. The predicted foot pressure can then be used in the optimization process. The second limitation is that the applied boundary conditions were not realistic. The out-of-plane displacement was fixed at the fore foot and at the heel part. The FO, on the other hand, is placed over the shoe which is made of a deformable material. Thus, the FO's displacement is not equal to zero on the heel part and on the fore foot. Adding an elastic foundation into the FE simulation might solve this issue. Yet, the adjustable parameters of that foundation should be experimentally determined. The third limitation is that the homogenized model is not able to accurately capture the maximum stress at the critical points of the FO with high stress concentrations. After the optimization process, it is recommended to predict the maximum von Mises stress by the explicit model and compare it with the material strength of the 3D printed FO. Moreover, fatigue fracture of the FOs should be taken into account since the FO is under a repeated loading (bending and torsion) during walking or running. In this regard, more experimental studies are required to understand the fatigue behavior of a 3D printed lattice FO during walking.

The fourth limitation of this work is that the predictions of the explicit and the homogenized models were not compared together within all the iterations of the optimization process. In Example #5, they were only compared at the final optimized solution. Based on our experience, it was difficult to write a computer program to automatically generate, mesh and update the FO CAD file to be used as the explicit FE model within the optimization iterations. The geometrical complexity of the honeycomb lattice FO is the main issue. Nevertheless, progressive development in CAD software along with open-source libraries in programming languages will enable to automatically re-create and re-mesh functionally graded honeycomb lattice FO. This might be also an interesting topic for the companies in

future works. Moreover, only two geometrical variables (ρ and h_2) were optimized in the designed FO. Adding more geometrical variables (such as T_1, T_2, L, h_1 or θ), however, leads to design more customized functionally graded FO. Yet, it increases the convergence time of the optimization and it may require more complex cost functions featuring regularization terms.

A fast optimization process and a rapid manufacturing procedure using 3D printers could potentially help orthotists to rapidly design, fabricate, and prescribe functionally graded lattice FOs for patients with flat feet deformities to enjoy comfortable walking or running.

5 Conclusion

We employed the homogenized model as a surrogate to accelerate the stiffness optimization of a honeycomb lattice FO for the flat foot condition. The homogenization technique enabled us to compute the effective properties of honeycomb cells and insert them into an equivalent and computationally efficient FE model featuring shell elements. Using shell elements rather than 3D solid elements significantly reduced the computational cost.

In an optimization of 18 geometrical variables of honeycomb lattice insole, the computational time was reduced from 34 days to 10 hours using the homogenized model rather than the explicit model. Moreover, the verification results showed that the homogenized model of the functionally graded honeycomb lattice FO is able to predict the local minimum out-of-plane displacement having a relative difference of less than 13%, when compared to the explicit model's prediction. The homogenization technique, therefore, provided a computationally efficient design tool to produce patient-specific FOs.

6 Declaration of competing interest

The authors declare that they have no known competing financial interests or personal relationships that could have appeared to influence the work reported in this paper.

7 CRediT author statement

Mohammadreza Moeini: Conceptualization, Methodology, Investigation, Software, Formal analysis, Writing - Original Draft. **Lingyu Yue**: Software, Writing - review & Editing. **Mickael Begon**: Conceptualization, Writing - review & Editing, Funding acquisition, Co-supervision. **Martin Lévesque**: Conceptualization, Writing - review & Editing, Resources, Funding acquisition, Supervision.

8 Acknowledgments

The authors greatly acknowledge Jacinte Bleau for sharing her valuable experiences in orthotics application, Maryam Hajizadeh and Gauthier Desmyttere to provide the measured pressure distribution of the flat foot and Anne-Laure Ménard to prepare the photo of the flat foot in Figure 1 and also for her helpful comments to write this paper. Moreover, this research was financially supported by NSERC R&D Coop with Medicus, Caboma and MEDTEQ [grant number RDCPJ 506194-16].

References

[1] Pita-Fernandez, S., Gonzalez-Martin, C., Alonso-Tajes, F., Seoane-Pillado, T., Pertega-Diaz, S., Perez-Garcia, S., Seijo-Bestilleiro, R., and Balboa-Barreiro, V. *Journal of clinical and diagnostic research: JCDR* **11**(4), LC22 (2017).

[2] Shibuya, N., Jupiter, D. C., Ciliberti, L. J., VanBuren, V., and La Fontaine, J. *The Journal of foot and ankle surgery* **49**(4), 363–368 (2010).

[3] Tahmasebi, R., Karimi, M. T., Satvati, B., and Fatoye, F. *Foot & ankle specialist* **8**(3), 168–174 (2015).

[4] Desmyttere, G., Hajizadeh, M., Bleau, J., and Begon, M. *Clinical Biomechanics* **59**, 117–129 (2018).

[5] Banwell, H. A., Thewlis, D., and Mackintosh, S. *The Foot* **25**(2), 101–109 (2015).

[6] Cheung, R. T., Chung, R. C., and Ng, G. Y. *British journal of sports medicine* **45**(9), 743–751 (2011).

[7] Gordillo-Fernández, L. M., Ortiz-Romero, M., Valero-Salas, J., Salcini-Macías, J. L., Benhamu-Benhamu, S., García-de-la Peña, R., and Cervera-Marin, J. A. *Prosthetics and orthotics international* **40**(6), 668–674 (2016).

[8] Xu, R., Wang, Z., Ren, Z., Ma, T., Jia, Z., Fang, S., and Jin, H. *Medical science monitor: international medical journal of experimental and clinical research* **25**, 3510 (2019).

[9] Telfer, S. and Woodburn, J. *Journal of foot and ankle research* **3**(1), 19 (2010).

[10] Desmyttere, G., Hajizadeh, M., Bleau, J., Leteneur, S., and Begon, M. *Clinical Biomechanics* **86**, 105390 (2021).

[11] Wang, Y., Tan, Q., Pu, F., Boone, D., and Zhang, M. *Engineering* (2020).

[12] Wang, X., Xu, S., Zhou, S., Xu, W., Leary, M., Choong, P., Qian, M., Brandt, M., and Xie, Y. M. *Biomaterials* **83**, 127–141 (2016).

[13] Lever, C. J. and Hennessy, M. S. *Orthopaedics and Trauma* **30**(1), 41–50 (2016).

[14] Hajizadeh, M. (2021).

[15] Peng, Y., Wong, D. W.-C., Chen, T. L.-W., Wang, Y., Zhang, G., Yan, F., and Zhang, M. *Computers in Biology and Medicine* **132**, 104355 (2021).

[16] Moeini, M., Ménard, A.-L., Yue, L., Hajizadeh, M., Begon, M., and Lévesque, M. *Computers in Biology and Medicine* , 105532 (2022).

[17] Hansen, N., Auger, A., Mersmann, O., Tusar, T., and Brockhoff, D. *arXiv preprint arXiv:1603.08785* (2016).

[18] Audet, C. and Hare, W. *Derivative-free and blackbox optimization*. Springer, (2017).

[19] Custódio, A. L., Madeira, J. A., Vaz, A. I. F., and Vicente, L. N. *SIAM Journal on Optimization* **21**(3), 1109–1140 (2011).

[20] Zhang, H., Wang, Y., and Kang, Z. *International Journal of Engineering Science* **138**, 26–49 (2019).

[21] Gao, J., Luo, Z., Li, H., and Gao, L. *Computer Methods in Applied Mechanics and Engineering* **344**, 451–476 (2019).

[22] Fu, J., Li, H., Gao, L., and Xiao, M. *Computers & Structures* **212**, 162–172 (2019).

[23] Robbins, J., Owen, S., Clark, B., and Voth, T. *Additive Manufacturing* **12**, 296–304 (2016).

[24] Ghossein, E. and Lévesque, M. *International Journal of Solids and Structures* **49**(11-12), 1387–1398 (2012).

[25] Moeini, M., Begon, M., and Lévesque, M. *Mechanics of Materials* , 104210 (2022).

[26] Audet, C. and Dennis Jr, J. E. *SIAM Journal on optimization* **17**(1), 188–217 (2006).

[27] Audet, C., Le Digabel, S., and Tribes, C. Technical report, Technical report G-2009-37, Les cahiers du GERAD, (2009).

[28] Le Digabel, S. *ACM Transactions on Mathematical Software (TOMS)* **37**(4), 1–15 (2011).

[29] Hajizadeh, M., Michaud, B., Desmyttere, G., Carmona, J.-P., and Begon, M. *PloS one* **15**(5), e0232677 (2020).

[30] Hajizadeh, M., Desmyttere, G., Ménard, A.-L., Bleau, J., and Begon, M. *Gait & Posture* **91**, 117–125 (2022).

[31] Malek, S. and Gibson, L. *Mechanics of Materials* **91**, 226–240 (2015).

[32] Divert, C., Mornieux, G., Freychat, P., Baly, L., Mayer, F., and Belli, A. *International journal of sports medicine* **29**(06), 512–518 (2008).

[33] Nielsen, R. G., Rathleff, M. S., Simonsen, O. H., and Langberg, H. *Journal of foot and ankle research* **2**(1), 1–7 (2009).

[34] Abdi, H. and Williams, L. J. *Wiley interdisciplinary reviews: computational statistics* **2**(4), 433–459 (2010).

[35] Deb, K., Pratap, A., Agarwal, S., and Meyarivan, T. *IEEE transactions on evolutionary computation* **6**(2), 182–197 (2002).

[36] Tang, L., Wang, L., Bao, W., Zhu, S., Li, D., Zhao, N., and Liu, C. *Journal of the Mechanical Behavior of Biomedical Materials* (2019).

[37] Jafarzadeh, E., Soheilifard, R., and Ehsani-Seresht, A. *Medical Engineering & Physics* **98**, 44–49 (2021).

[38] Schaper, N., Van Netten, J., Apelqvist, J., Lipsky, B., Bakker, K., and on the Diabetic Foot (IWGDF), I. W. G. *Diabetes/metabolism research and reviews* **32**, 7–15 (2016).

[39] Cherni, Y., Desmyttere, G., Hajizadeh, M., Bleau, J., Mercier, C., and Begon, M. *Clinical Biomechanics* , 105553 (2021).

A Verification of the optimized solution

The verification of results consists in comparing the predicted out-of-plane displacement by the homogenized model featuring the optimized stiffness resulting from Example #5 against that of its explicit model. Figure 13 shows the optimized parameters of Example #5 within the FO's domain. In all sub-domains, the side length was fixed to $l_b^{(i)} = 2.0$ and the wall thickness $t^{(i)}$ was computed by Equation 1 having the optimized relative density of $\rho^{(i)}$ where $i \in \{1, \ldots, 9\}$. The optimized FO is presented in Figure 14a-e. However, as shown in details A-C, there are some discontinuities between the sub-domains due to their different cell topologies, which makes its meshing procedure difficult. In the *modified version* (Figure 14f-j), the borders are filled with solid bars having a width of 2 mm. Moreover, the holes at the top surface of the FO were removed. Correspondingly, these modifications are also added to the homogenized model (Figure 14k-o). Figure 15 indicates the comparison of the predicted displacement field by the homogenized model against that of the explicit model for the *modified version*. The maximum discrepancy between the predictions (*i.e.*, $\frac{|U_Z^{\mathrm{Hmg}} - U_Z^{\mathrm{E}}|}{\max |U_Z^{\mathrm{E}}|}$) is 29.6%. Among the selected lines, the maximum discrepancy is $\xi = 12.45\%$ in line $G - H$ (Figure 16). Yet, the predictive capability of the homogenized model might be still accepted due to the required computational cost to run the explicit model.

B Convergence study of the mesh refinement

Figure 17 shows the convergence study of the mesh refinement in Example #5. The element sizes of the explicit, as well as the homogenized model, were uniformly refined as $\frac{l_{\mathrm{element}}}{l_b} = 8$, 4, 2, 1, 0.9, 0.8, 0.7, ..., in which $l_b = 2.0\,\mathrm{mm}$ (see also Figure 13). The refinement was stopped when:

$$\bar{\Delta} U_{Z\min} = \frac{U_{Z\min}^{\mathrm{fine}} - U_{Z\min}^{\mathrm{coarse}}}{U_{Z\min}^{\mathrm{fine}}} \leq 0.005, \tag{14}$$

where $\bar{\Delta} U_{Z\min}$ returns the relative difference between the predicted minimum out-of-plane displacement with a fine mesh ($U_{Z\min}^{\mathrm{fine}}$) against the predicted one by a coarse mesh ($U_{Z\min}^{\mathrm{coarse}}$).

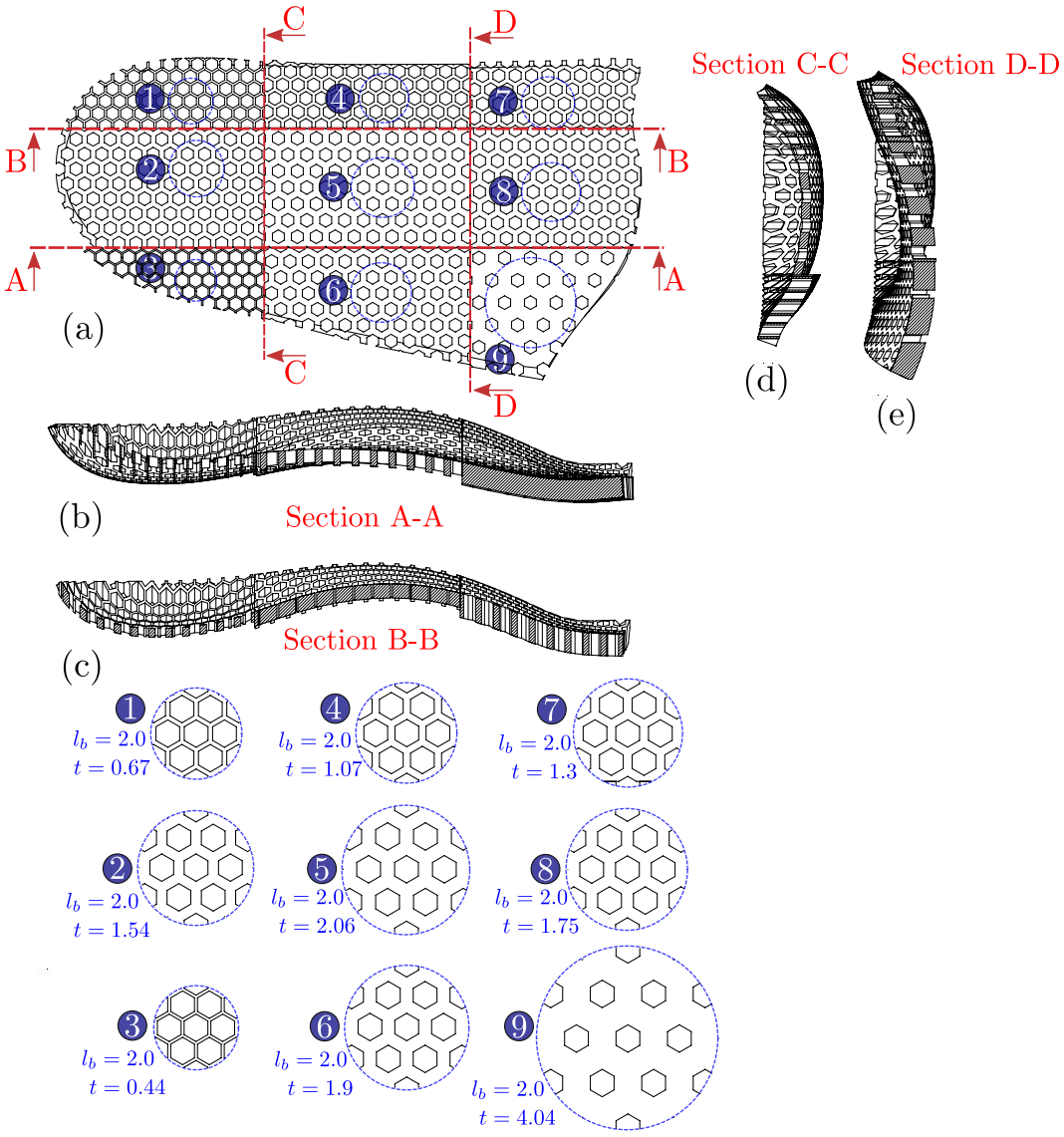

Figure 13: Schematic representation of the optimized parameters ρ^* and h_2^* in the nine sub-domains resulting from the optimization Example #5; (a) the main structure, (b) cross-section A-A, (c) cross-section B-B, (d) cross-section C-C and (e) cross-section D-D. Each sub-domain has been extruded by the optimized height of $h_2^{(i)}$ and cut-extruded by a hexagonal pattern regarding the optimized relative density of $\rho^{(i)}$ where $i \in \{1, \dots, 9\}$. Note that the relative density depends on parameters l_b, h_b, l, h and θ according to Equation 1. We already considered only regular hexagons in which $l_b = h_b$, $l = h$ and $\theta = \pi/6$. Moreover, the length side was considered $l_b^{(i)} = 2.0\,\text{mm}$ for all $i \in \{1, \dots, 9\}$. Consequently, solving Equation 1 having the optimized relative density returns the wall thickness $t^{(i)}$ for $i \in \{1, \dots, 9\}$.

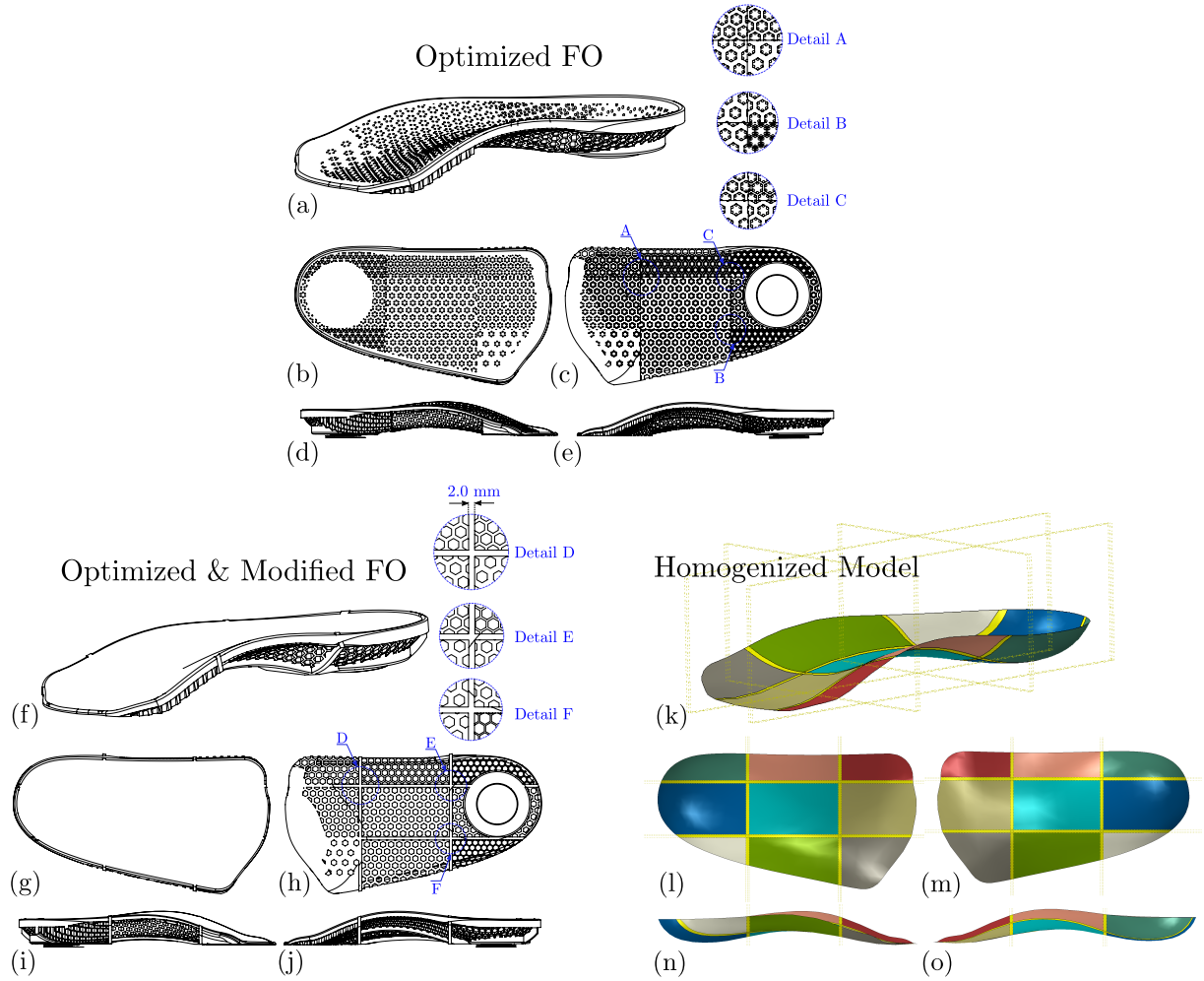

Figure 14: Optimized FO geometry in Example #5; (a-e) the optimized FO, (f-j) the optimized and modified FO, (k-o) the homogenized model of the optimized and modified FO. In the optimized FO, each sub-domain features a different height and relative density which come from the optimized solution. The holes in the first layer correspond to hexagonal patterns. Thus, in each sub-domain, the holes pattern is different. The optimized FO had to be modified due to the discontinuity between the sub-domains having different honeycomb cells topologies and, correspondingly, due to the difficulties in meshing the geometry. In the modified FO, the holes at the first layer were removed. Moreover, the borders between the sub-domains have been filled with solid bars with a thickness of 2 mm. In the same way, in the corresponding homogenized FO, the first layer was considered as an in-filled layer and the borders were added whose mechanical properties were the bulk mechanical properties.

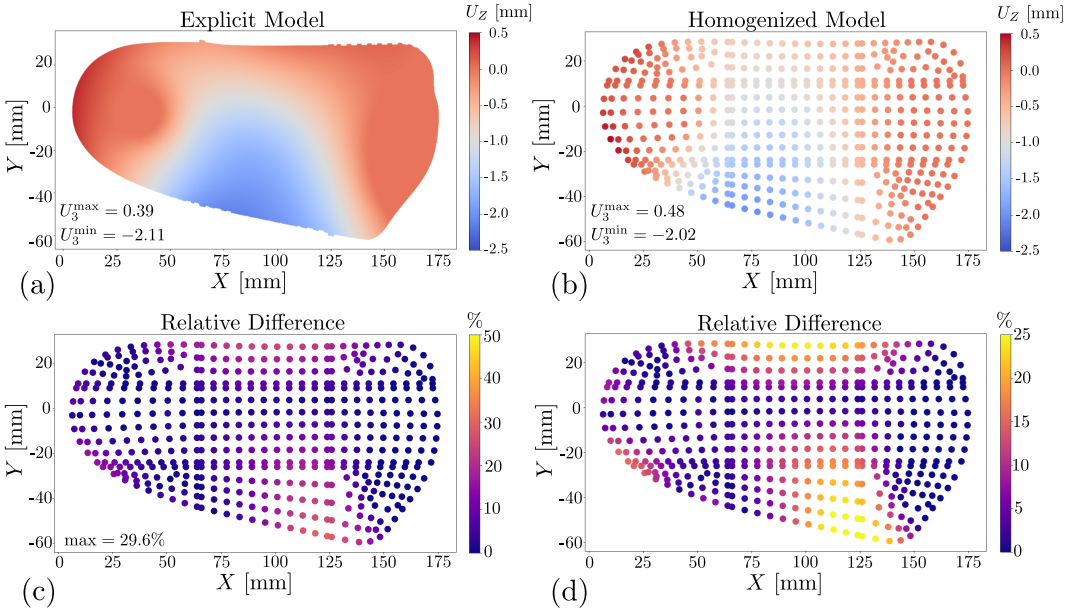

Figure 15: Comparison of the predicted displacement fields by the explicit model and the homogenized model of the optimized and modified FO resulting from Example #5; (a) the predicted displacement U_Z by the explicit model, (b) the predicted displacement U_Z by its homogenized model, (c) the computed relative difference between the predictions normalized by the maximum predicted U_Z by the explicit model (*i.e.* $\frac{|U_Z^{\text{Hmg}} - U_Z^{\text{E}}|}{\max |U_Z^{\text{E}}|}$) of within a range of $0 - 50\%$, (d) within a range of $0 - 25\%$ to show better its variation. The discrepancy is higher around the edge between $70 \leq X \leq 125$ and $10 \leq Y$ as well as around the forefoot ($100 \leq X \leq 130$ and $Y \leq -40$) where the boundary conditions were applied. In both cases, the discrepancy may come from the edge effect in the explicit model of the functionally graded honeycomb lattice FO.

The element type in the explicit model was 10-node 3D solid element (*i.e.*, `C3D10`). Furthermore, the convergence of the homogenized model was studied by two element types, including 4-node shell element (*i.e.*, `S4R`) and 8-node shell element (*i.e.*, `S8R5`). The result shows that the explicit model required 660 084 degrees of freedom (DOF) for convergence, while the homogenized model required 45 054 DOF for `S4R` elements or 128 196 DOF for `S8R5` element.

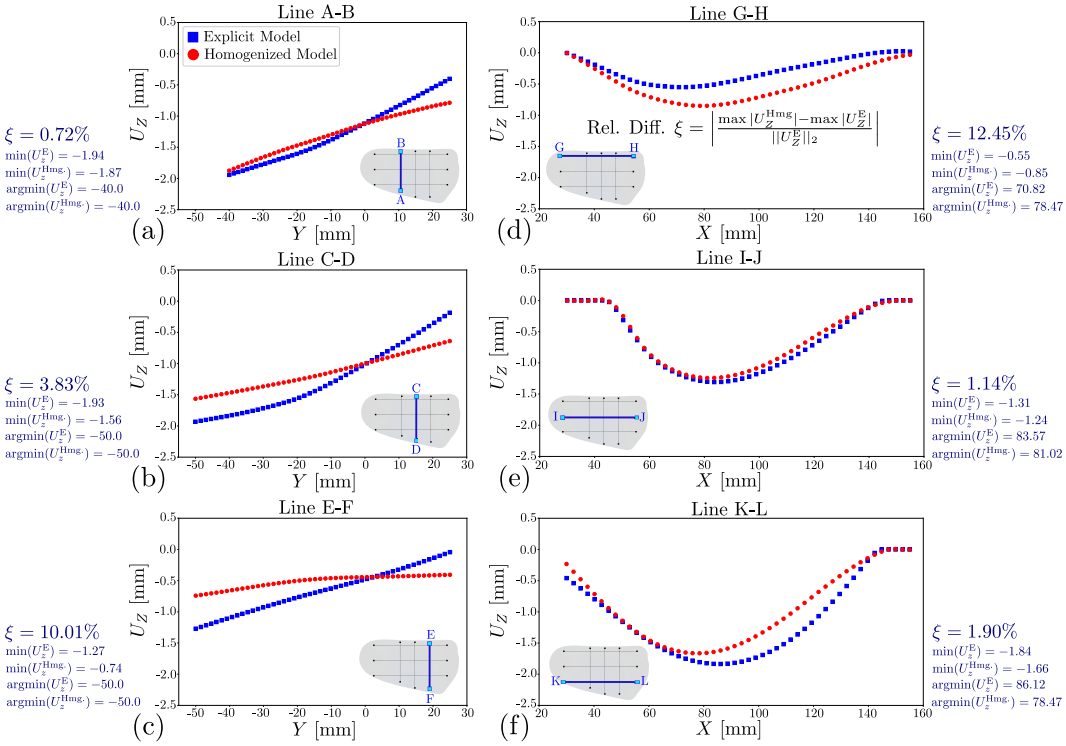

Figure 16: Comparison of the predicted displacement fields U_Z by the explicit model and the homogenized model of the optimized and modified FO resulting from Example #5 at lines; (a) (A, B), (b) (C, D), (c) (E, F), (d) (G, H), (e) (I, J) and (f) (K, L). The coordinates of the points in the three vertical lines are $A = (75, -40)$, $B = (75, 25)$, $C = (100, -50)$, $D = (100, 25)$, $E = (125, -50)$, $F = (125, 25)$, mm and in the three horizontal lines they are $G = (30, 20)$, $H = (155, 20)$, $I = (30, -5)$, $J = (155, -5)$, $K = (30, -30)$, $L = (155, -30)$ mm. The maximum discrepancy is over the line (G, H) in which $\xi = 12.45\%$.

C Using a large number of evaluations

In this appendix, Examples #1, #2, #3, #4 and #6 are solved within a sufficiently large number of evaluations and without stopping criteria of $\Delta^m_{\min}$ and $\Delta^p_{\min}$ to investigate the resulting optimized solution. In Examples #1 and #2, Figures 18 and 19 show that the solutions are stable after 25 evaluations and the optimal solutions remain the same. In Example #3, the cost function was reduced from 0.31 to 0.08 (*i.e.*, 74% improvement) when 1000 evaluations are given as the budget. Similarly, in Example #4, the cost function was reduced from 0.11 to 0.04 (*i.e.*, 64% improvement) after 1000 evaluations. Increasing the number of evaluations numerically increases the accuracy of the optimized solution. We accepted the

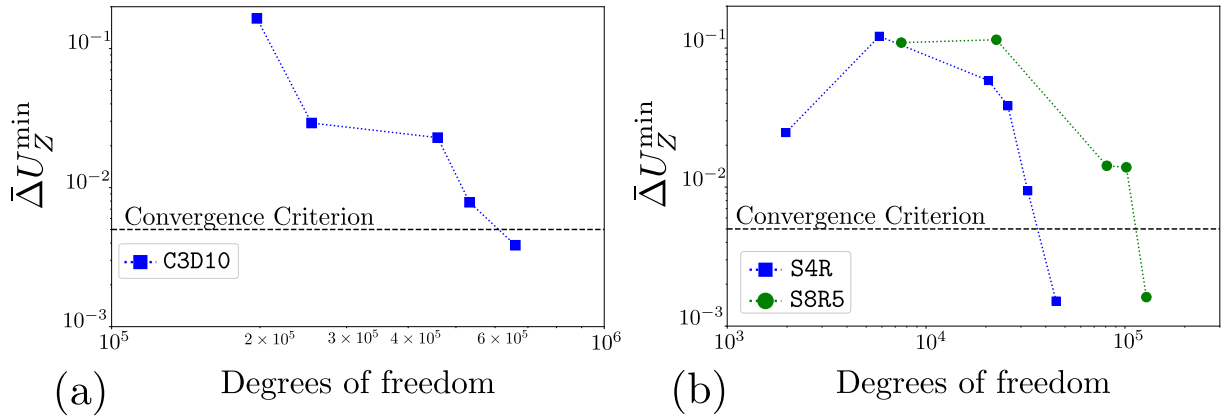

Figure 17: Mesh size convergence study for (a) the explicit model and (b) the homogenized model in optimization Example #5. The explicit model consisted of 3D solid elements (`C3D10`) and the homogenized model included 4-node (`S4R`) and 8-node (`S8R5`) shell elements. In both models, the element sizes were uniformly reduced to satisfy the convergence criterion of Equation 14.

results Example #3 and #4 from the stopping criterion of minimum mesh size since the predicted displacement from the optimized FO was very close to the reference displacement. In Example #3, imposing a minimum mesh size returns $\max(|U_Z^* - U_Z^{\mathrm{R}}|) = 0.06\,\mathrm{mm}$, while stopping by the maximum number of evaluations leads to $\max(|U_Z^* - U_Z^{\mathrm{R}}|) = 0.02\,\mathrm{mm}$. In Example #4, imposing a minimum mesh size returns $\max(|U_Z^* - U_Z^{\mathrm{R}}|) = 0.02\,\mathrm{mm}$, while stopping by the maximum number of evaluations leads to $\max(|U_Z^* - U_Z^{\mathrm{R}}|) = 0.01\,\mathrm{mm}$.

In Example #6, Figure 22 shows the resulting Pareto front after 8000 evaluations (almost 46 hours). The result shows that the Pareto front is remarkably improved when compared to the previous solution in which 1000 evaluations were allocated (Figure 12a). For instance, in this solution, the solver found $(f^{(1)}, f^{(2)}) = (1.24, 91.56)$ rather than $(f^{(1)}, f^{(2)}) = (5.06, 91.59)$ in the previous solution. Thus, the first cost function related to the stiffness is reduced by 75% using almost the same amount of the apparent mass. Furthermore, the resulting Pareto front includes more options to choose from (the solver found 366 points rather than 107 points in the previous solution). In this optimization, the computational time, however, is significantly increased (from 5 hours to 46 hours). The computational budget should be determined based on the time limitations to deliver the FOs or the required

accuracy of the optimized solution.

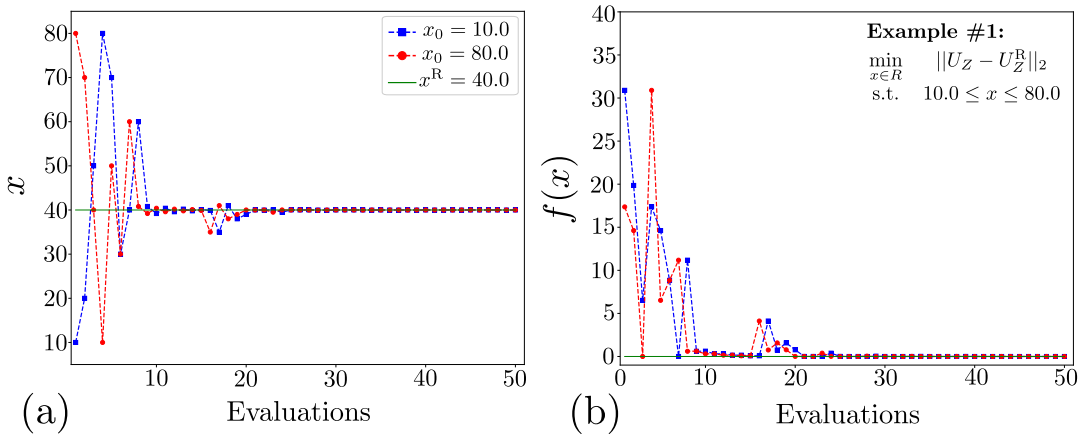

Figure 18: Variations of (a) x and (b) $f(x)$ with respect to the number of evaluations in optimization Example #1, in which the single variable was the relative density ρ and the objective was to minimize $||U_Z - U_Z^{\mathrm{R}}||_2$. In this solution, the maximum number of evaluations was increased to $\mathrm{N_{Eval}} = 50$ having no other stopping criterion. The initial points were considered as $x_0 = 10$ and $x_0 = 80$. In both cases, the optimal solutions are equal to the reference solution.

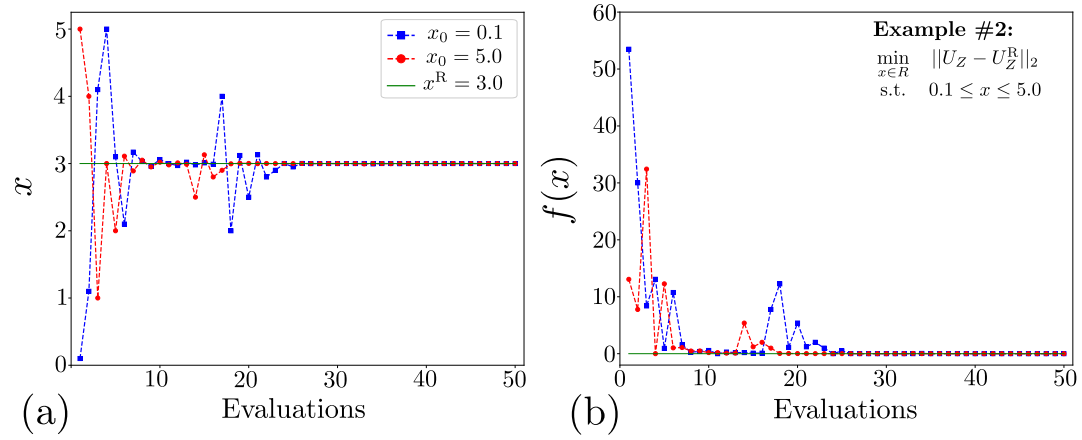

Figure 19: Variations of (a) x and (b) $f(x)$ with respect to the number of evaluations in optimization Example #2, in which of the single variable was the height of the cells and the objective was to minimize $||U_Z - U_Z^{\mathrm{R}}||_2$. In this solution, the maximum number of evaluations was increased to $\mathrm{N_{Eval}} = 50$ having no other stopping criterion. The initial points were considered as $x_0 = 0.1$ and $x_0 = 80$. In both cases, the optimal solutions are equal to the reference solution.

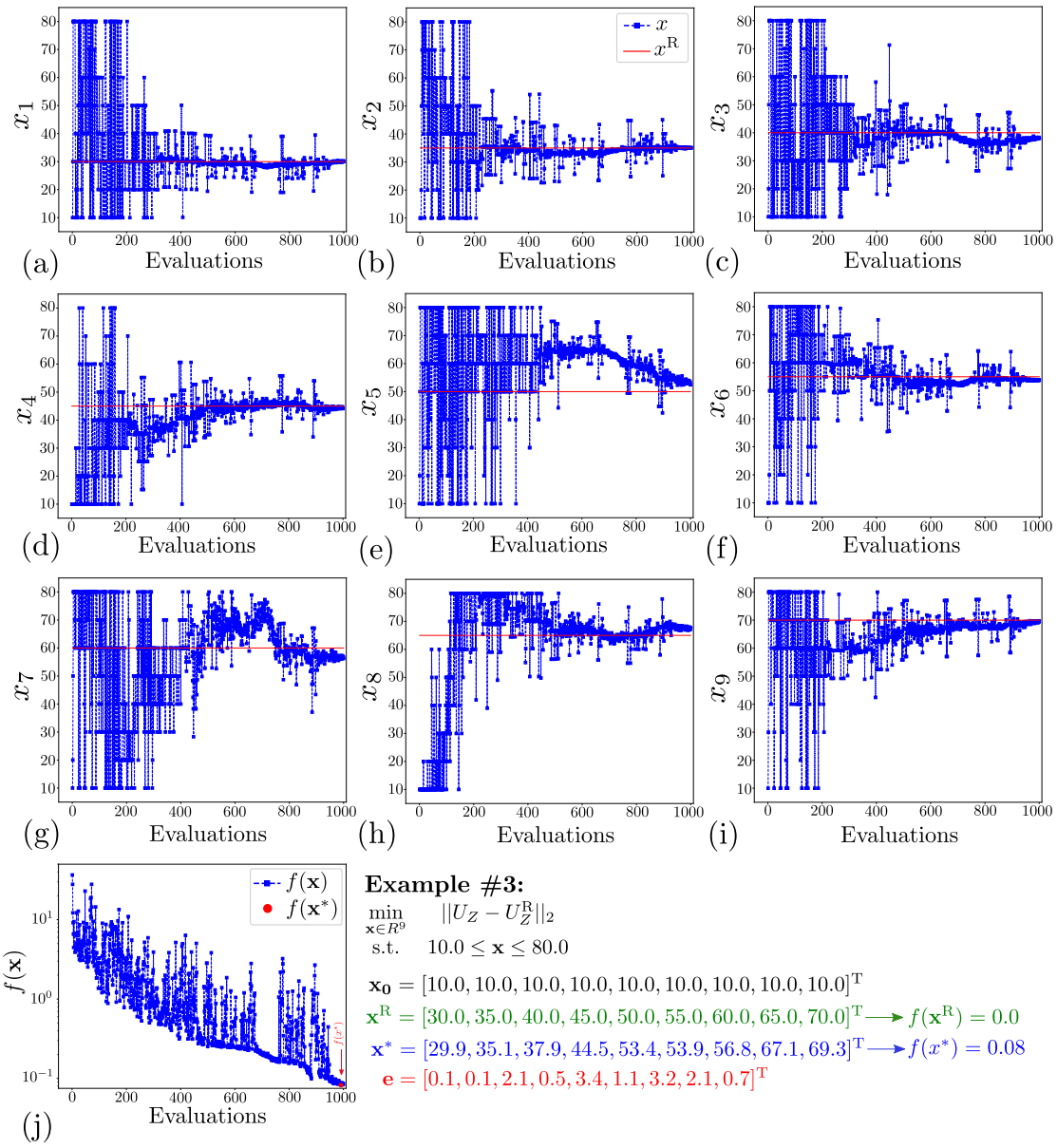

Figure 20: Variations of (a-i) x_i and (j) $f(\mathbf{x})$ in a log scale and with respect to the number of evaluations in optimization Example #3, in which the multiple variables were the relative densities of the cells at nine sub-domains and the objective was to minimize $||U_Z - U_Z^{\mathrm{R}}||_2$. In this solution, the maximum number of evaluations was increased to $\mathrm{N_{Eval}} = 1000$ having no other stopping criterion. The optimal solution has a maximum absolute error of 3.4% in domain 5 and the minimized cost function was 0.08.

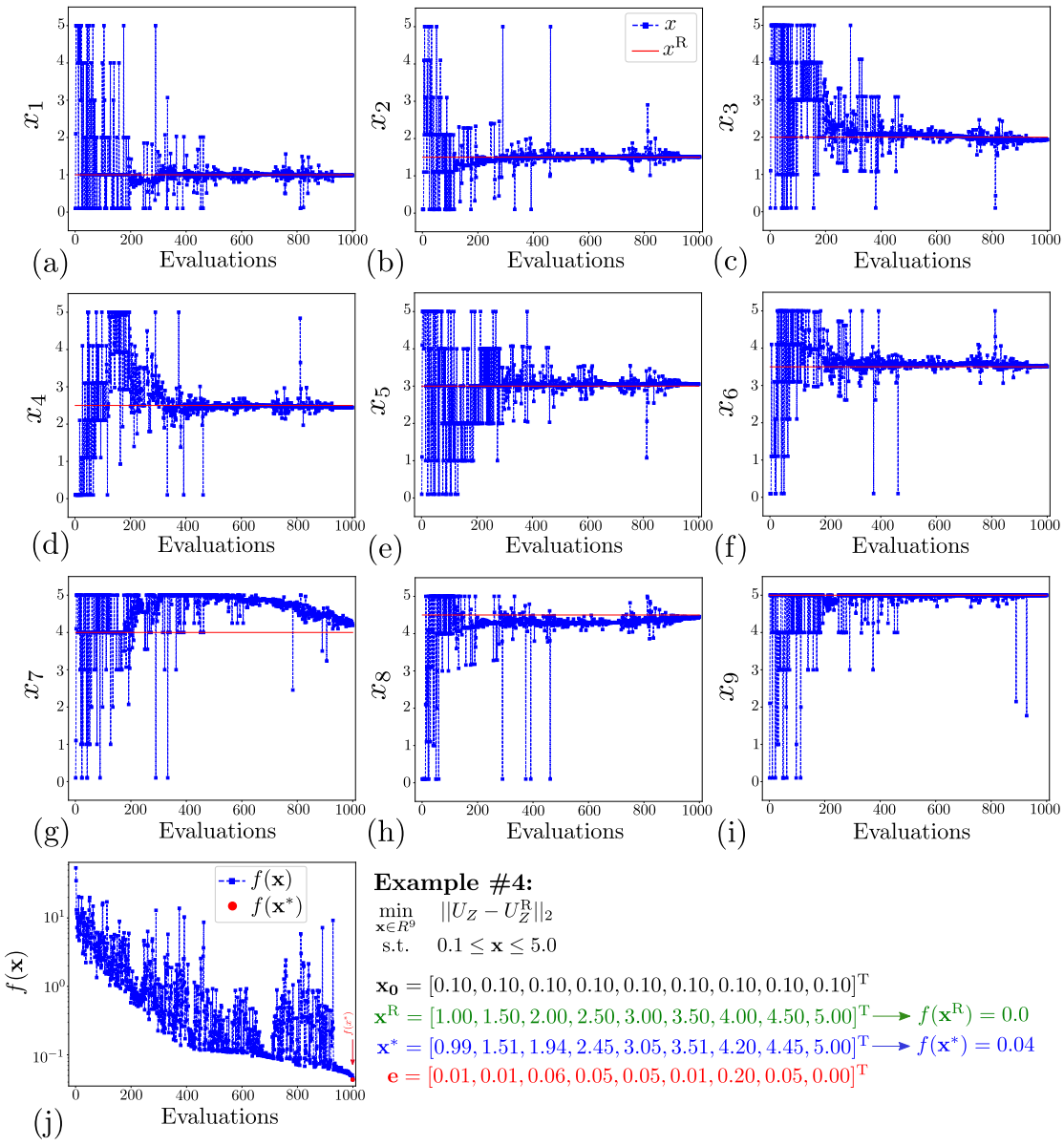

Figure 21: Variations of (a-i) x_i and (j) $f(\mathbf{x})$ in a log scale and with respect to the number of evaluations in optimization Example #4, in which the multiple variables were the heights of the cells at nine sub-domains and the objective was minimization of $||U_Z - U_Z^{\mathrm{R}}||_2$. In this solution, the maximum number of evaluations was increased to $\mathrm{N_{Eval}} = 1000$ having no other stopping criterion. The optimal solution has a maximum absolute error of 0.2 mm in domain 7 and the minimized cost function was 0.04.

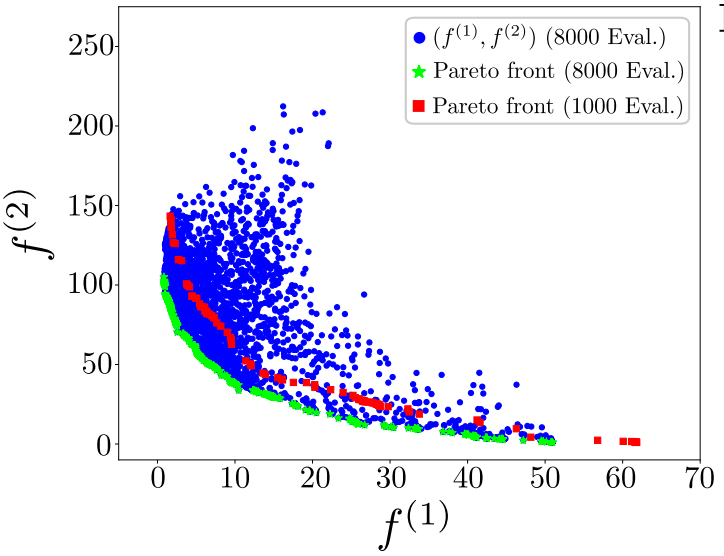

Example #6:

$$\min_{\mathbf{x}\in R^{18}} \quad F(\mathbf{x}) = \left(f^{(1)}(\mathbf{x}), f^{(2)}(\mathbf{x})\right)$$

$$f^{(1)} = ||U_Z - U_Z^{\mathrm{R}}||_2$$

$$f^{(2)} = \frac{1}{\sum_i a^{(i)}} \sum_i \rho^{(i)} h_2^{(i)} a^{(i)}$$

$$\mathbf{x} = [\rho^{(1)}, \ldots, \rho^{(9)}, h_2^{(1)}, \ldots, h_2^{(9)}]^{\mathrm{T}}$$

$$\text{s.t.} \quad 0.1 \leq h_2^{(i)} \leq 5.0$$

$$10.0 \leq \rho^{(i)} \leq 80.0$$

$$\delta_i - 4.0 \leq 0.0$$

$$i \in \{1, 2, \ldots, 9\}$$

Figure 22: Evaluated cost functions and the Pareto front in Example #6 with 8000 evaluations. Increasing the number of evaluations from 1000 to 8000 improves the results. By improvement we mean that the Pareto front consists of lower values of $(f^{(1)}, f^{(2)})$ (as it can be seen from the figure) and it also includes more optimal points. Allowing 1000 evaluations returns 107 optimal solutions, while giving 8000 evaluations returns 366 optimal solutions. Solving an optimization problem with 8000 evaluations, however, takes almost 46 hours. The decision maker should address whether the computational time is a priority or the accuracy of the optimal solutions.